OUKA
Osaka University Knowledge Archive

Title	Defect structures and electrical properties of perovskite-type oxides
Author(s)	Yoshioka, Hideki
Citation	大阪大学, 1999, 博士論文
Version Type	VoR
URL	https://doi.org/10.11501/3155642
rights	
Note	

Osaka University Knowledge Archive : OUKA

https://ir.library.osaka-u.ac.jp/

Osaka University

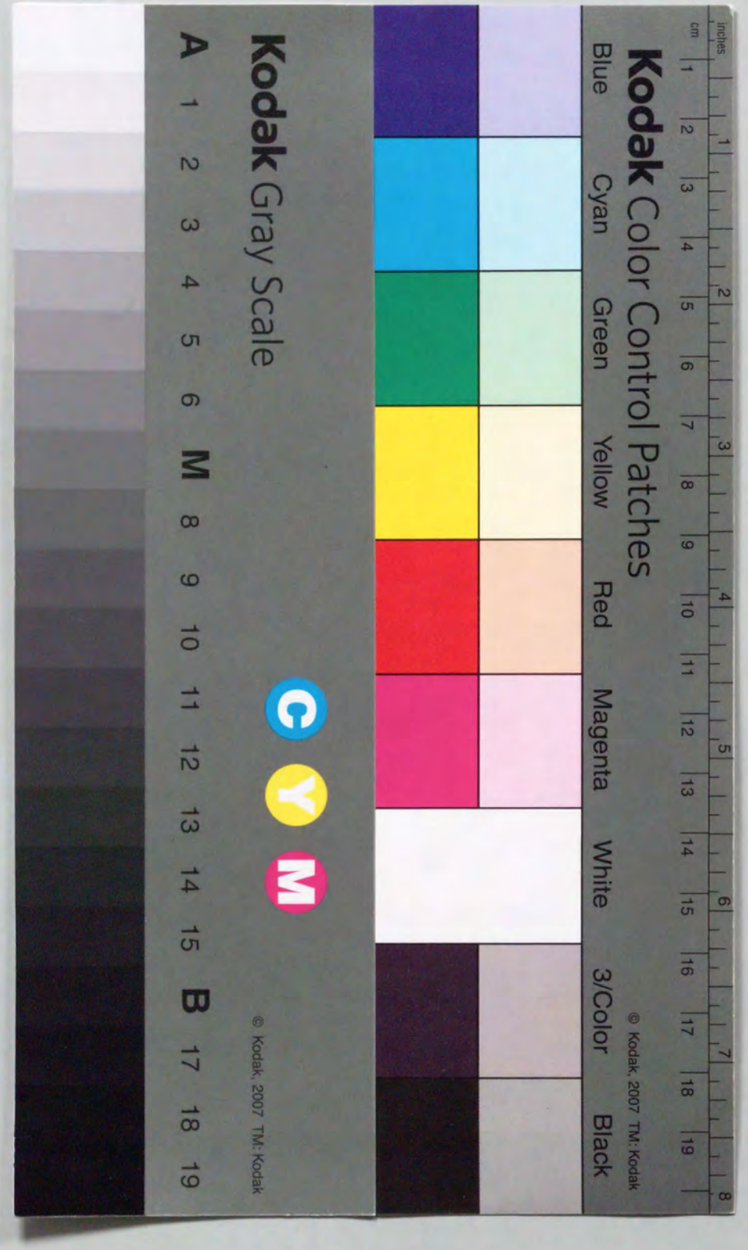

Defect structures and electrical properties of perovskite-type oxides

（ペロブスカイト型酸化物における欠陥構造と電気的性質）

1999

Hideki YOSHIOKA

Defect structures and electrical properties of perovskite-type oxides

（ペロブスカイト型酸化物における欠陥構造と電気的性質）

1999

Hideki YOSHIOKA

Contents

General introduction 1

1 Electrical properties and defect structures of $PbTiO_3$-$MgTiO_3$ solid solutions prepared by the sol-gel method 7

2 Dielectric anomaly and ionic conduction in A-site deficient La-Ti-Al-O perovskites 24

3 Sol-gel preparation and defect structures of thin films in $PbTiO_3$-$La_{2/3}TiO_3$ solid solutions 48

4 Rapid quenching and dielectric properties of $Pb(Mg_{1/2}W_{1/2})O_3$ 64

5 High pressure synthesis of Bi-Sr-Ca-Cu-O superconductors 80

Conclusions 93

List of publications 96

Acknowledgments 98

General introduction

Purpose of this study

Point defects in solids greatly affect their properties. The purpose of this study is to elucidate the relationship between defect structures and electrical properties in the perovskite-type oxides. Formation of solid solutions, introduction of lattice vacancies and ordering of these defects are studied in connection with the dielectric properties, ionic conduction and superconducting properties. New processing techniques such as sol-gel method, rapid quenching method and high pressure synthesis are explored in view of enhancing the defect concentration and controlling the defect ordering.

Defects in perovskite-type oxides

The perovskite structure is one of the most important structures for advanced oxide materials [1]. There exist two cation sites in the perovskite structure, 12 fold A-site and 6 fold B-site [2]. A wide variety of cation combinations which offers an opportunity for successful materials design are possible [3]. In addition, most of properties can be controlled continuously by partial substitutions for both cation sites. For example, the Curie points of ferroelectric perovskite-type oxides such as $BaTiO_3$ and $PbTiO_3$ can be shifted over a wide range of temperature [4]. Another example is enhancement in the electrical and ionic conductivity by the substitution with different valent cations which introduce conductive electrons, holes or lattice vacancies [5].

Site preferences of the substituting ions which are added to form solid solutions are determined by their valences and ionic radii [5]. Low valent cations (+1-+3) with large ionic radii such as alkaline metal ions and alkaline earth metal ions substitute for A-site cations; higher valent cations (+3-+5) with small ionic radii substitute for B-site

cations. Some divalent ions such as Mg^{2+}, Zn^{2+} and Ni^{2+} have small ionic radii and thus, in general, are hardly soluble in the perovskite structure [6, 7]. Site preferences and effects on the properties are of interest if the solubilities of these ions are increased. The enhancement of the solubility is investigated in this study using new processing techniques as discussed below.

With an increase in the defect concentration, an interaction between defects sometimes gives rise to defect ordering which greatly affects the electrical properties. A little was known, however, about the relation between the defect ordering and the electrical properties.

One of the examples is an effect of cation ordering on the dielectric properties of the complex perovskite-type oxides. Setter and Cross [8] showed that ordering of B-site cations, Sc^{3+} and Ta^{5+}, in $Pb(Sc_{1/2}Ta_{1/2})O_3$ can be changed by heat treatment. The compound subjected to high temperature heat treatment had a random arrangement of the B-site cations and showed a broad relaxer-type ferroelectric transition. After heat treatment at a lower temperature for a long period of time the transition turned into a sharp one because of the ordering of the B-site cations. Also, dielectric loss at microwave frequencies in $Ba(Zn_{1/3}Ta_{2/3})O_3$ ceramics was reported to decrease with increased Zn and Ta ordering [9].

Another example is oxide ion conduction in the deficient perovskite-type oxides. Both oxide ion vacancy and its random arrangement enhance the oxide ion conductivity. Barium indium oxide, $BaInO_{2.5}$, has 1/6 of ordered oxide ion vacancy and thus shows considerable oxide ion conductivity. Random arrangement in the oxide ion vacancy which is achieved by the partial substitution for In sites by Zr increases oxide ion conductivity significantly [10].

New processing techniques

In the sol-gel method, starting materials are well-mixed in the liquid state and then heat-treated at a low temperature to form a product. This process makes it possible to prepare amorphous or metastable phases without causing crystallization or

phase separation [11]. These phases are considered to have an ability of holding more defects than the stable crystalline phases. Therefore enhancement of defect and vacancy concentrations is expected on the samples prepared by the sol-gel method.

By the rapid quenching technique, uniform glasses have been obtained for a number of oxides which crystallize at a normal cooling rate [12]. Metastable phases which are prepared by crystallization from the glasses at low temperatures are expected to have a lot of defects as is similar in the case of the sol-gel method.

Under high pressure phase stability is different. High pressure syntheses have been successfully carried out to form metastable phases of inorganic materials including oxides [13]. Consequently we have a chance to introduce more defects and make particular defect structures by high pressure syntheses.

Methods and materials

Figure 1 shows methods used and materials investigated in this study. Materials are typical functional oxides which have well-defined electrical properties and simple perovskite-type structures so that clear results on the effects of defect structures can be elucidated.

The methods are as follows:

(1) Defects are introduced as much as possible to the typical functional perovskite-type oxides. The sol-gel method, rapid quenching method and high pressure synthesis are used to enhance the defect concentration.

(2) Heat treatments are conducted to change the defect ordering. This process also promotes crystallization from amorphous phases, formation of superstructures and phase separation.

(3) The electrical properties (dielectric properties, electrical conductivity, ionic conductivity and superconductivity) are measured. The relationship between the defect arrangement and electrical properties are examined.

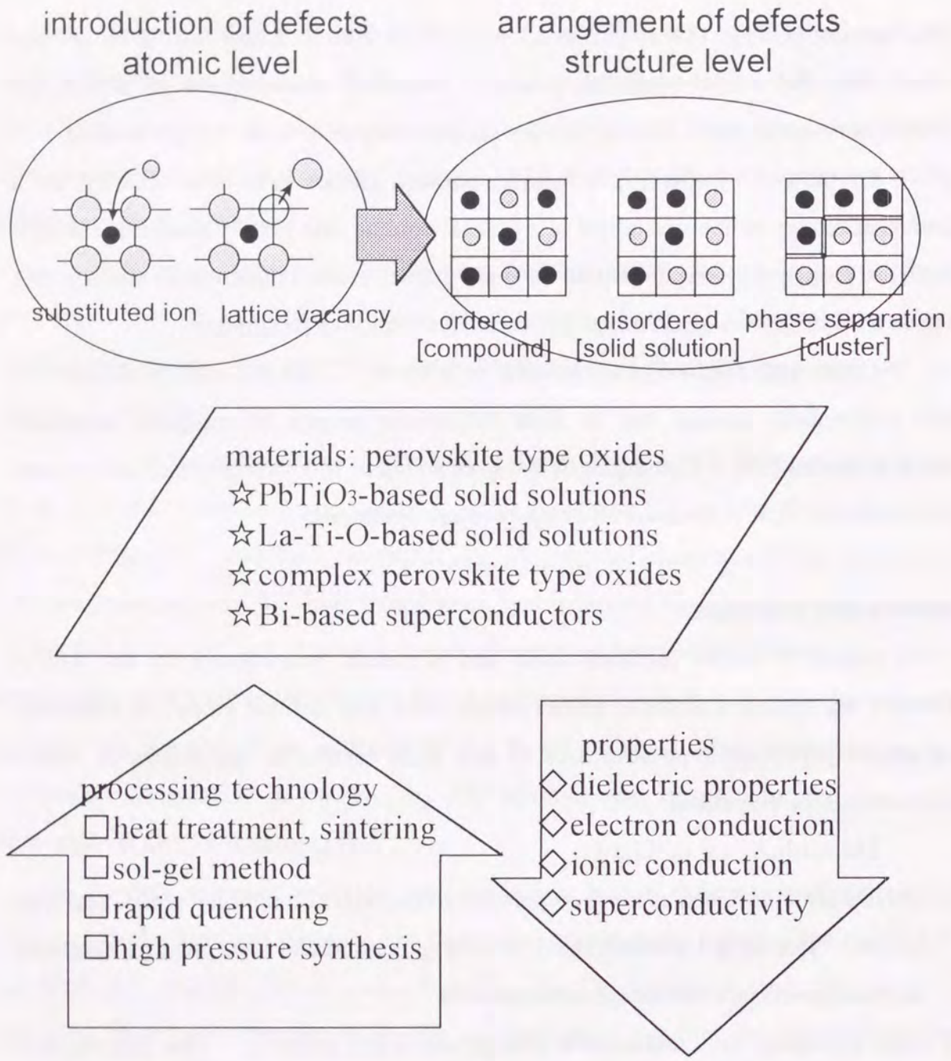

Fig. 1 Methods and materials in this study.

Contents

This chapter presents the purpose, methods and materials in this study. Chapter 1 shows the results on the sol-gel preparation of $PbTiO_3$ - $MgTiO_3$ solid solutions and their electric properties. The sol-gel method is found to be effective to enhance the solubility of Mg^{2+} in the perovskite structure. The defect structure of the solid solution is clearly shown from the changes in the electrical properties with different atmospheres.

Chapter 2 deals with the deficient perovskite $La_{2/3}TiO_3$ with one third of the A-site cation vacancy. It is found that the perovskite structure is stabilized by the partial substitution for Ti^{4+} by Al^{3+}. A strong relation between the cation vacancy ordering and oxide ion conductivity is noted to show that the defect ordering brings about the new function in this material.

Thin film preparation for $PbTiO_3$-$La_{2/3}TiO_3$ solid solutions is reported in chapter 3. It is found that the perovskite phase forms in the sol-gel derived films of all compositions even for pure $La_{2/3}TiO_3$ with one third of cation vacancy. The $La_{2/3}TiO_3$ film showed much lower conductivity than bulk ceramics of La-Ti-Al-O. This is explained from the difference in the defect structure.

The rapid quenching of an antiferroelectric complex perovskite oxide, $Pb(Mg_{1/2}W_{1/2})O_3$, is described in chapter 4. The formation of the amorphous phase, crystallization by heat treatments, change in the defect structure and dielectric properties due to the phase transformation are investigated in relation with defect structures.

In chapter 5, high pressure synthesis of Bi-based superconductors is studied. High pressure synthesis from the mixed oxide powders and phase change under high pressure are explored to reveal the effect of pressure on the structure and the superconducting properties.

In conclusions, the relations between processing methods, defect structures and electrical properties in the perovskite-type oxides are discussed from above results.

References

1 F. S. Galasso, "Structure, Properties and Preparation of Perovskite-type Compound", Pergamon, Oxford (1969).

2 F. Kanamaru, "KIKAN KAGAKU SOSETSU 32, Perovskite-Related Compounds: Storehouse of Functions", p.7, ed. the Chemical Society of Japan, Gakkai Shuppan Center, Tokyo (1997).

3 M. Shimada, *ibid*, p.3 (1997).

4 T. Mitsui, E. Nakamura, K. Gesi, T. Ikeda, Y. Makita, M. Marutake, S. Nomura, E. Sawaguchi, T. Shigenari, Y. Shiozaki, I. Tatsuzaki, K. Toyoda, M. Adachi, J. Harada, T. Shiosaki, K. Wakino and T. Yamada, "Landort - Börnstein", New Series, GroupIII, vol. 16b, Springer (1982).

5 J. Mizusaki, "KIKAN KAGAKU SOSETSU 32, Perovskite-Related Compounds: Storehouse of Functions", p.24, ed. the Chemical Society of Japan, Gakkai Shuppan Center, Tokyo (1997).

6 P. Baxter, N. J. Hellicar and B. Lewis, *J. Amer. Ceram. Soc.*, **42**, 465 (1959).

7 T. Y. Tien and W. G. Carlson, *J. Amer. Ceram. Soc.*, **45**, 567 (1962).

8 N. Setter and L. E. Cross, *J. Appl. Phys.*, **51**, 4356 (1980).

9 S. Kawashima, M. Nishida, I. Ueda and H. Ouchi, *J. Amer. Ceram. Soc.*, **66**, 421 (1983).

10 J. B. Goodenough, J. E. Ruiz-Diaz and Y. S. Zhen, *Solid State Ionics*, **44**, 21 (1990).

11 S. Sakka, *Chemistry and Chemical Industry*, **45**, 906 (1992).

12 T. Minami, *Ceramics Japan*, **17**, 278 (1982).

13 O. Fukunaga, *ibid*, **32**, 452 (1997).

Electrical properties and defect structure of $PbTiO_3$-$MgTiO_3$ solid solutions prepared by the sol-gel method

1.1 Introduction

Lead titanate ($PbTiO_3$) has a tetragonal perovskite structure with a ferroelectric Curie temperature of 763 K [1]. Owing to the high Curie temperature, it is an attractive material for high-temperature and high-frequency applications. However, the preparation of pure dense $PbTiO_3$ ceramics with a high resistivity is difficult because of Pb volatilization occurred during the sintering and a large internal strain which is induced when cooling below the Curie temperature. A number of solid solutions have been studied in order to improve mechanical and electric properties of $PbTiO_3$ [2]. It has been found that large divalent cations such as Ba^{2+}, Ca^{2+}, Sr^{2+} enter the A-site of the perovskite lattice; trivalent or quadrivalent cations with small ionic radii such as Al^{3+}, Zr^{4+}, Sn^{4+} and heavy rare earth ions substitute for the B-site cations. The solubility of Mg^{2+} in $PbTiO_3$ was proved to be very small in an equilibrium stable state [3], because ionic radius of Mg^{2+} is too small to occupy the A-site and a number of cation vacancies must be introduced with the substitution for the B-site to maintain charge balance.

In this chapter, the sol-gel method is used to prepare $PbTiO_3$-$MgTiO_3$ (PMT) solid solutions. Improved compositional homogeneity and a lower firing temperature involved in the sol-gel method favor the formation of metastable solid solutions and thus enlarge the solubility limit. Dielectric properties and electrical conductivity in various atmospheres are investigated in order to elucidate the defect structure of the solid solutions and the site preference of Mg^{2+} in the perovskite structure.

1.2 Experimental

Starting materials were titanium tetraisopropoxide (TIP), lead(II) acetate [$Pb(OCOCH_3)_2 \cdot 3H_2O$], and magnesium(II) acetate [$Mg(OCOCH_3)_2 \cdot 4H_2O$]. Compositions ranging from x = 0 to 0.5 for $(1\text{-}x)PbTiO_3\text{-}xMgTiO_3$ were studied as listed in Table 1.1. All samples were prepared as shown in Fig. 1.1. Triethanolamine (TEA) was used both to increase the solubility of acetates and to avoid the precipitation on hydrolysis [4]. An appropriate amount of TEA, lead acetate and magnesium acetate were dissolved in the TIP-ethanol solution; the molar ratio of TIP to ethanol was 1/8. The necessary amount of water which had been diluted twice with ethanol was then added dropwise under vigorous stirring. The transparent, highly viscous sols were obtained. The amount of water needed to gelation depended on the composition of the mixed solutions.

Table 1.1 Compositions (molar ratio) for sol-gel preparation of $PbTiO_3$-$MgTiO_3$

$Pb(OCOCH_3)_2 \cdot 3H_2O$	$Mg(OCOCH_3)_2 \cdot 4H_2O$	TIP	TEA	H_2O
1.00	0.00	1.00	0.50	17
0.98	0.02	1.00	0.50	24
0.95	0.05	1.00	0.50	28
0.90	0.10	1.00	0.50	30
0.80	0.20	1.00	0.50	32
0.67	0.33	1.00	0.50	32
0.50	0.50	1.00	0.40	20

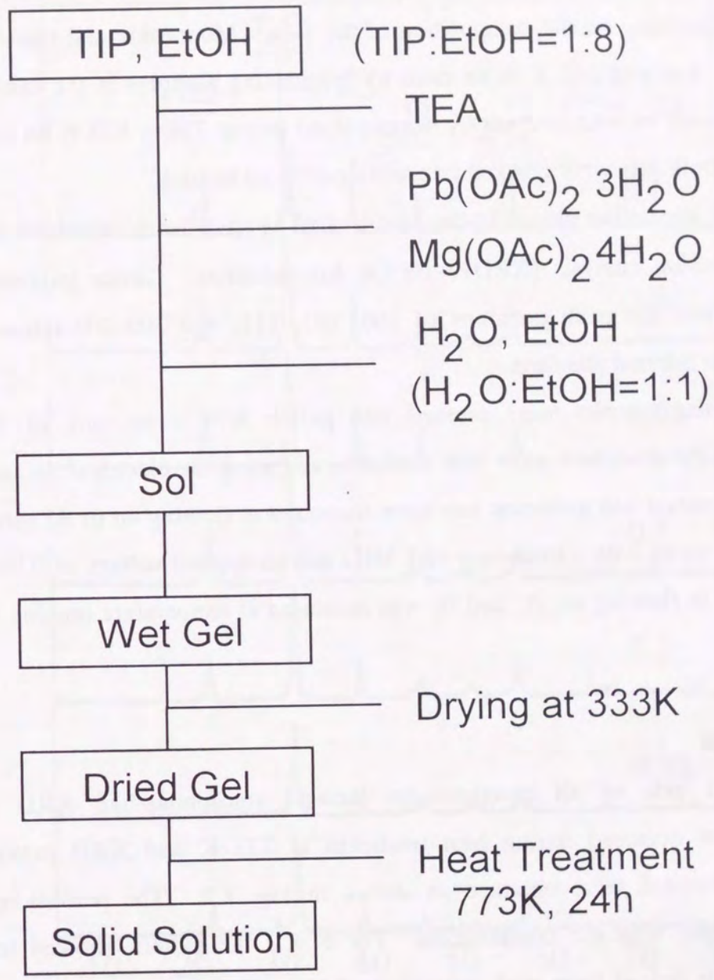

Fig. 1.1 Flow chart for the sol-gel preparation of $PbTiO_3$-$MgTiO_3$ solid solutions.

The sols were poured into a polystyrene container, sealed and allowed to stand for gelling at room temperature. It required several minutes to several hours for the gelation, depending on the composition of the sols. Monolithic and translucent gels were dried slowly at 333 K in an oven by introducing pinholes in the container cap. Heat treatments were carried out by heating dried gels at 773 or 823 K for 24 h. The monolithic bulk gels were cracked into small pieces on heating.

The crystalline phases in the heat-treated samples were examined by powder X-ray diffraction analysis (XRD) with Cu Kα radiation. Lattice parameters were calculated from the peak positions of 100, 101, 111, and 200 diffraction using Si powder as an internal standard.

Powder samples were pressed into pellets with a pressure of 150 MPa, sputtered Pt-Pd electrodes onto both surfaces, and used for electrical measurements. Dielectric constant and dielectric loss were measured in flowing air or Ar using a YHP 4275A LCR meter with a frequency of 1 MHz and an applied voltage of 0.05 V. DC conductivity in flowing air, Ar and O_2 was measured at temperature ranging from 603 to 753 K.

1.3 Results

Dried gels of all compositions showed amorphous-like XRD patterns. Crystallization occurred during heat treatment at 773 K and XRD patterns of a perovskite structure were obtained as shown in Fig. 1.2. The perovskite pattern slightly changes with the composition. For x = 0 the pattern showed tetragonal symmetry as is judged from peak separation of 100 and 001, 101 and 110 and so on. The tetragonality decreased with increasing x.

Figure 1.3 shows a change in the 002 and 200 diffraction lines with the composition. It is observed that the 002 line shifts to a higher angle and the 200 to a lower angle with increasing x. It is also revealed that peak width of the 002 is much larger than that of the 200; this is evident as x increases to 0.02 and 0.05. Above x = 0.2 the separation of 002 and 200 is not clear. Thus we could identify the 200 peak

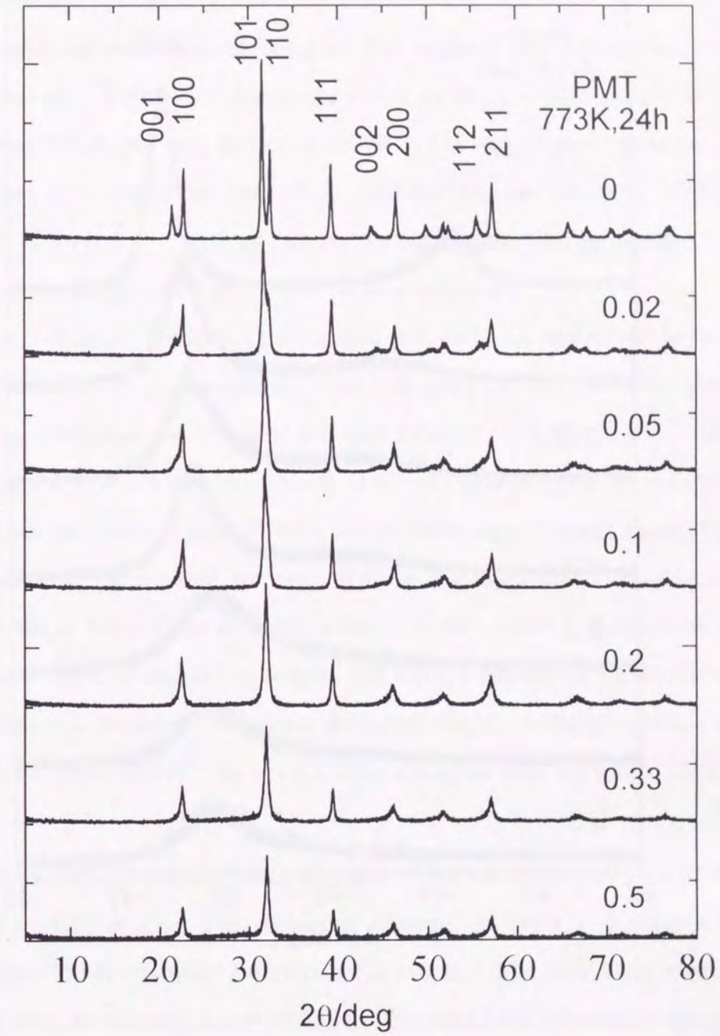

Fig. 1.2 X-ray diffraction patterns of sol-gel derived (1-x)$PbTiO_3$-$x$$MgTiO_3$ heated at 773 K for 4 h.

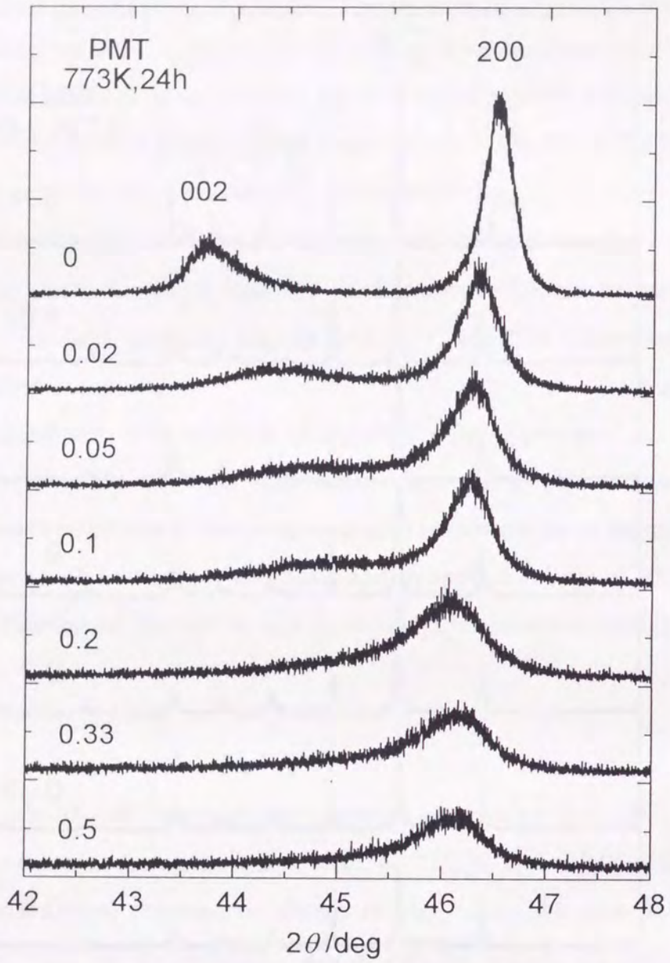

Fig. 1.3 002 and 200 diffraction peaks of sol-gel derived (1-x)$PbTiO_3$-$x$$MgTiO_3$ heated at 773 K for 24 h.

positions only. The significant asymmetric character, however, is noticed in these 200 peaks with $0.2 \leq x \leq 0.5$.

The obtained perovskite phases gave rise to phase separation when heated at a higher temperature. Figure 1.4 shows the result on the $x = 0.33$ sample which were first prepared at 773 K and then heated at 973 K. The single-phase perovskite pattern (a) decomposes to a tetragonal perovskite, $PbTiO_3$, and an ilmenite, $MgTiO_3$, with heating at 973 K for 0.5 h. With an increase in the heating time an amount of $MgTiO_3$ as well as the tetragonality of a perovskite structure increase.

Figure 1.5 shows the lattice parameters and the cubic root of the lattice volume ($V^{1/3}$) as a function of the composition. The symmetry of the perovskite phases were assumed to be tetragonal for $0 \leq x \leq 0.1$ and cubic for $0.2 \leq x \leq 0.5$. The lattice parameters for $x = 0$ ($a = 0.3912$ nm, $b = 0.4149$ nm) were in good agreement with the published values for single crystal $PbTiO_3$ ($a = 0.3904$ nm, $c = 0.4152$ nm) [5]. The c value decreases and the a value increases with increasing x up to 0.1; especially, the marked decrease in the c value is noted when x is very small. A decrease in $V^{1/3}$ is also observed when x is small; but it does not change linearly with the composition. When x exceeds 0.2, the lattice parameter decreases slightly with increasing x up to 0.5. It should be also noted that $V^{1/3}$ for $x \leq 0.1$ does not agree with the lattice parameter for $x \geq 0.2$.

Figure 1.6 shows the dielectric constant of the tetragonal samples ($0 \leq x \leq 0.1$) measured at 1 MHz in air. The dielectric constant of the $x = 0$ sample increases markedly above 700 K, showing a maximum at 780 K. The maximum temperature is in agreement with the Curie point of $PbTiO_3$. The dielectric properties changed much with the composition. For $x = 0.02$ the values of the dielectric constant decreases over wide range of temperature; the Curie point moves to the lower temperature and the dielectric peak is very wide. Above $x = 0.05$ the dielectric maximum due to the Curie point is hardly observed.

The dielectric loss for $x = 0$ in Fig. 1.6 increases at a high temperature after showing a maximum at the Curie point. This is a typical loss behavior of the

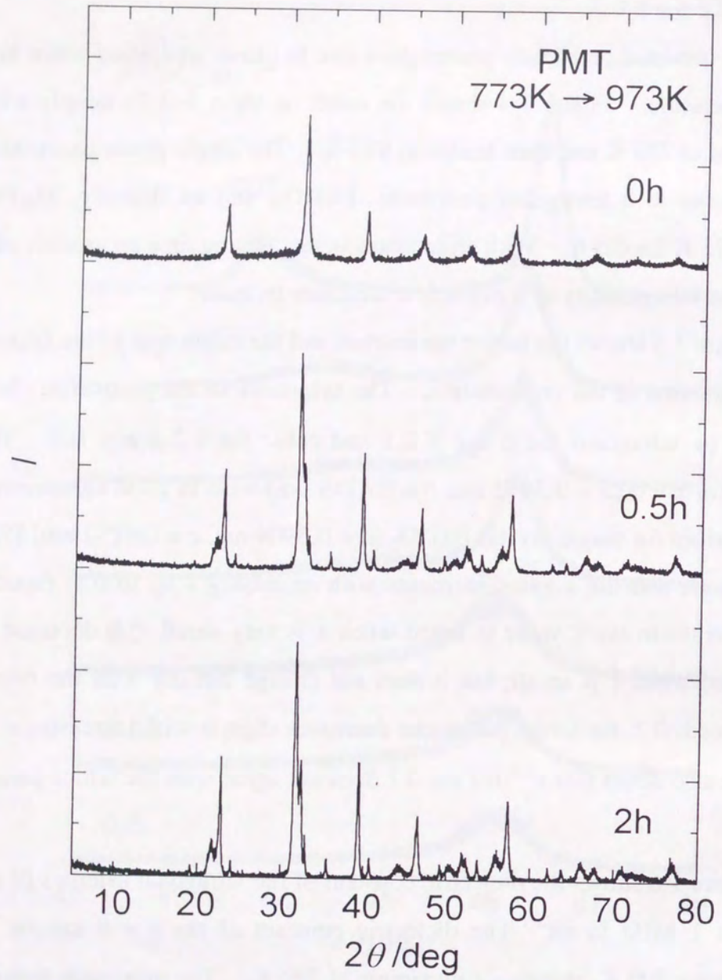

Fig. 1.4 XRD patterns of sol-gel derived $0.67PbTiO_3$-$0.33MgTiO_3$ after the post heat treatment at 973 K.

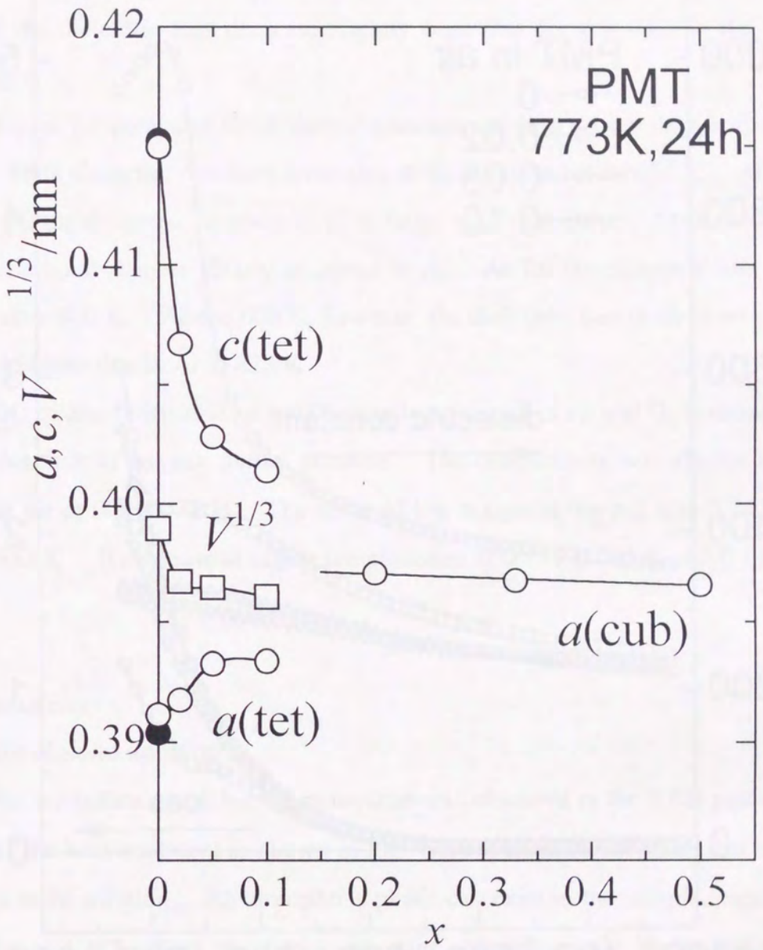

Fig. 1.5 Lattice parameters and cubic root of lattice volume of sol-gel derived $(1\text{-}x)PbTiO_3$-$xMgTiO_3$ powders.

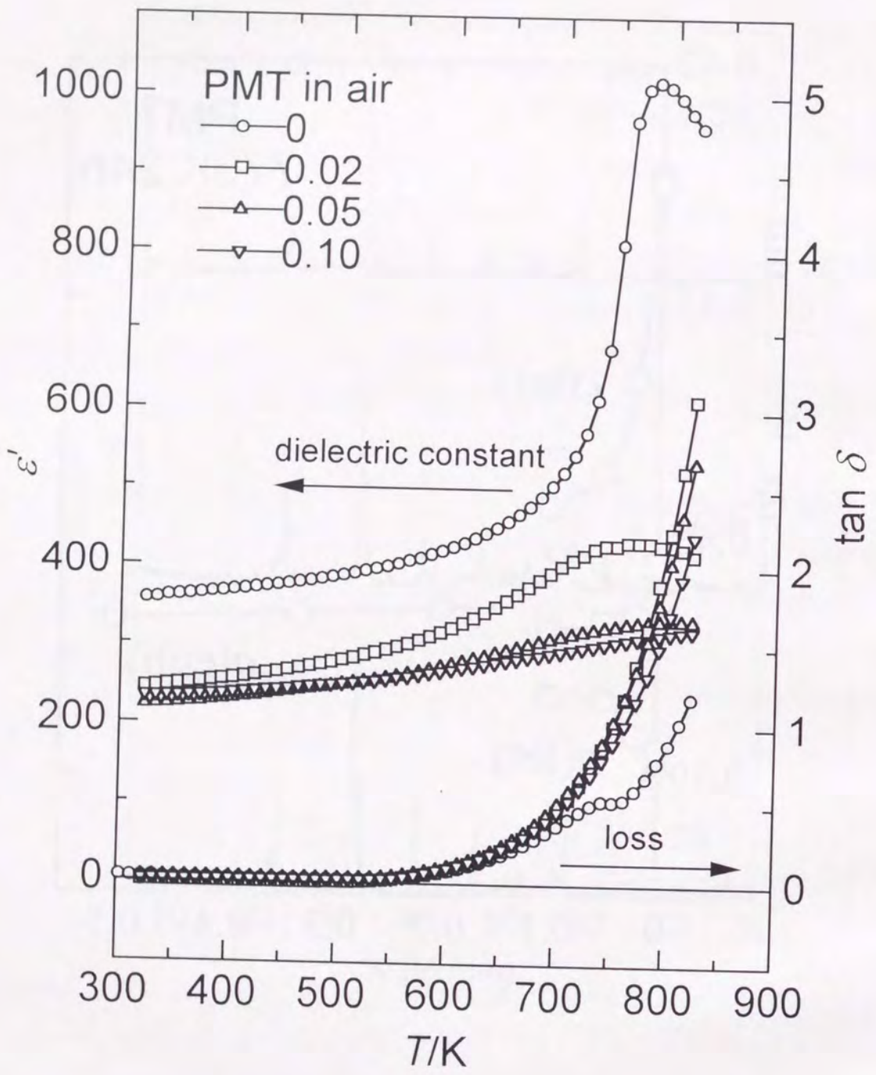

Fig. 1.6 Dielectric constant and dielectric loss of sol-gel derived $(1\text{-}x)PbTiO_3$-$xMgTiO_3$ with $0 \leq x \leq 0.1$ heated at 773 K for 24 h.

ferroelectric phase transition. The dielectric loss for $x = 0.02$ is evidently higher than that for $x = 0$, showing no maximum and simply increasing at high temperature. The values of the dielectric loss decrease slightly from that for $x = 0.02$ in the order of increasing x.

Figure 1.7 compares the dielectric constant and loss for $x = 0.05$ in flowing air and Ar. Both dielectric constants have almost same values below 600 K. Above 600 K, however, the dielectric constant in air is larger than that in Ar. Also, the peak due to the Curie point is more clearly observed in Ar. As for the dielectric loss they are similar below 600 K. Above 600 K, however, the dielectric loss in air is much larger; it is about 3times that in Ar at 823 K.

DC conductivity of the $x = 0.05$ sample measured in air and O_2 is shown in Fig. 1.8 as a function of oxygen partial pressure. The conductivity was always higher in O_2 than in air at 603 - 753 K. The slope of log σ against log p_{O2} was 0.242 both at 603 and 653 K. It decrease at higher temperatures as 0.177 at 703 K and 0.126 at 753 K.

1.4 Discussion

Formation of solid solution

No crystalline phase but the perovskite was observed in the XRD patterns for $x \leq 0.5$ after the heat treatment as shown in Fig. 1.2. This does not mean that all added Mg forms solid solution. An amorphous phase can exist in the sample, especially in the region $x \geq 0.2$ where the lattice constant showed a little dependence on the composition (Fig. 1.5). Since the relative diffraction intensities are also very similar, it is considered that the composition in the perovskite phases above $x = 0.2$ does not change so much. In contrast, in the tetragonal region of small x, the lattice parameters changed greatly with x as shown in Fig. 1.5. The dielectric properties near the Curie point also showed a large dependence on x as shown in Fig. 1.6. These indicate the formation of solid solution in the tetragonal region.

Single crystals of $PbTiO_3$ - MgO solid solutions were grown by Kobune *et al.*[3)]

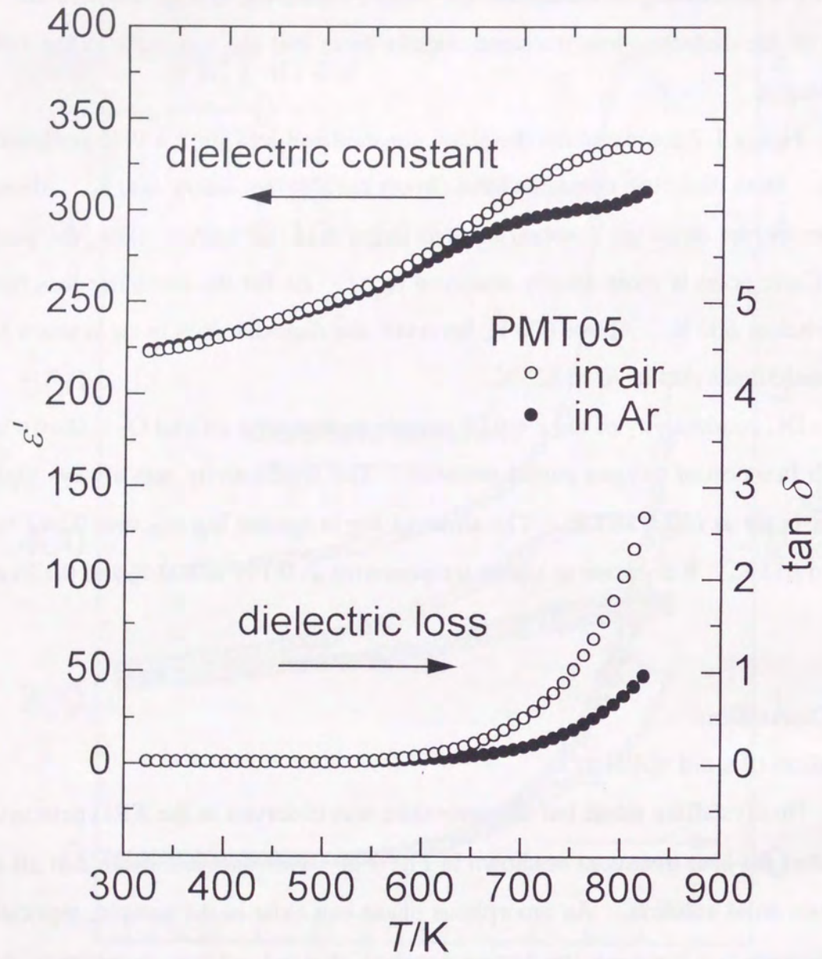

Fig. 1.7 Dielectric constant and dielectric loss of sol-gel derived $0.95PbTiO_3$-$0.05MgTiO_3$ measured in flowing air and Ar.

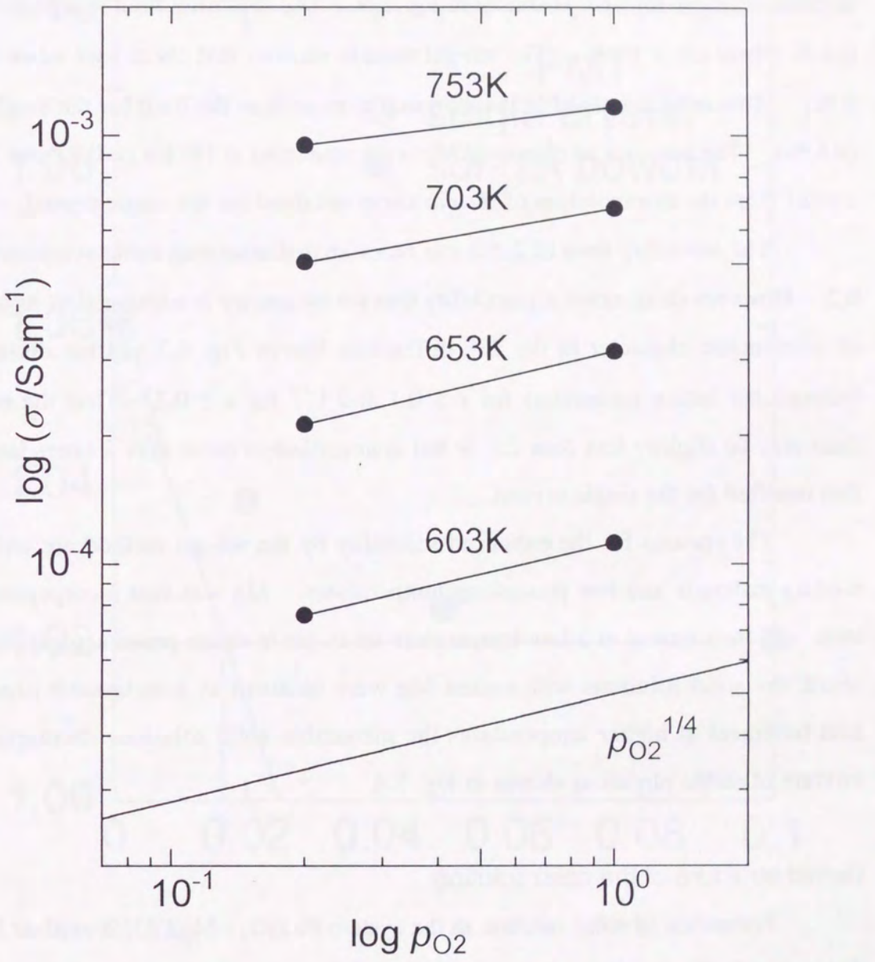

Fig. 1.8 DC conductivity of sol-gel derived $0.95PbTiO_3$-$0.05MgTiO_3$ as a function of an oxygen partial pressure.

According to their XRD results the lattice parameter along *a*-axis increased slightly and that for *c*-axis decreased greatly with the addition of MgO; the tetragonality (*c*/*a*) decreased almost linearly as shown in Fig. 1.9. The solubility limit was reported to be 0.6 % where $c/a = 1.045$. The sol-gel sample showed that $c/a \leq 1.04$ when $0.02 \leq x \leq 0.1$. This indicates that Mg is incorporated more than the limit for the single crystal (0.6 %). The amounts of dissolved Mg were estimated at 1% for $x = 0.02$ and 1.7% for $x = 0.1$ from the extrapolation of the *c*/*a* curve obtained for the single crystal.

The solubility limit of 2.5% can be estimated assuming cubic symmetry for $x \geq 0.2$. However there exists a possibility that the symmetry is tetragonal as judged from an asymmetric character in the 200 diffraction line in Fig. 1.3 and the disagreement between the lattice parameters for $x \leq 0.1$ and $V^{1/3}$ for $x \geq 0.2$. Thus the solubility limit may be slightly less than 2.5 % but is nevertheless more than 3 times larger than that reported for the single crystal.

The reasons for the enhanced solubility by the sol-gel method are well-mixed starting materials and low processing temperatures. Mg was first incorporated in gel state, and then heated at a low temperature so as not to cause phase separation. As a result, the solid solutions with excess Mg were obtained as a metastable phase. By heat treatment at higher temperatures the metastable solid solutions decomposes to a mixture of stable phases as shown in Fig. 1.4.

Defect structure of the solid solution

Formation of solid solution in the system $PbTiO_3$ - $MgTiO_3$ is evident from the discussion in the previous section. Two models were examined as a defect structure of the solid solutions based on the fact that Mg^{2+} is a divalent cation and it has a small ionic radius.

(A) Mg^{2+} enters the A-site: $(Pb_{1-x}Mg_x)TiO_3$

(B) Mg^{2+} enters the B-site: $(Pb_{1-x}\square_{2x})(TiMg_x)O_3\square_{2x}$

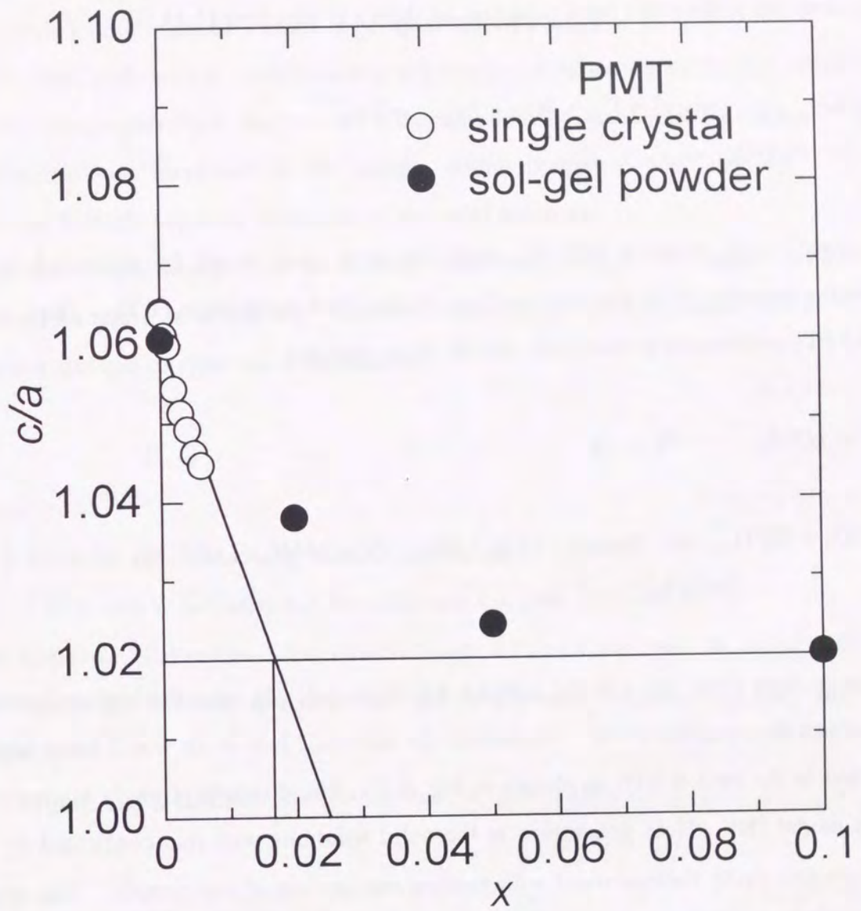

Fig. 1.9 Tetragonality (*c*/*a*) of $(1-x)PbTiO_3$-$xMgTiO_3$ single crystal and sol-gel powder as a function of *x*.

The model (A) is a simple substitution reaction in which dielectric properties would change slightly with the composition. The model (B) requires the A-site and oxide ion vacancies to form the solid solutions as shown in equation (1.1).

$$MgTiO_3 \xrightarrow[PbTiO_3]{} Mg_{Ti}'' + Ti_{Ti} + 3O_O + 2V_{Pb}'' + 3V_O^{\bullet\bullet} \qquad (1.1)$$

If oxygen in air is taken into the oxide vacancy, hole would be generated as the following equation (1.2) and total reaction is described as equation (1.3). Thus, in the model (B), an increase in dielectric loss in air is expected.

$$V_O^{\bullet\bullet} + 1/2\ O_2 \rightarrow O_O + 2h^{\bullet} \qquad (1.2)$$

$$MgTiO_3 + 3/2\ O_2 \xrightarrow[PbTiO_3]{} Mg_{Ti}'' + Ti_{Ti} + 6O_O + 2V_{Pb}'' + 6h^{\bullet} \qquad (1.3)$$

As can be seen from Fig. 1.6, the samples which include Mg have the higher dielectric loss values than that for $x = 0$. Moreover, the dielectric loss in air was 3 times higher than that in Ar for $x = 0.05$ as shown in Fig. 1.7. These results strongly support the defect model (B). Hole generation in the solid solutions was also confirmed by an electromotive force measurement with heating one surface of the sample. The result indicates *p*-type conduction.

The mass-action expression for the equation (1.2) combined with the charge-neutrality condition gives $\sigma \propto p_{O2}^{1/4}$ which coincides with the results observed in Fig. 1.8 below 653 K. This result also supports the model (B). The slope of log σ against log p_{O2} decreased above 703K. This is probably due to partial reduction of Ti^{4+} ion at high temperature in air which cause a decrease in hole concentration.

1.5 Summary

(1) Mg ion could be dissolved in the sol-gel derived powder of $PbTiO_3$-$MgTiO_3$. The solubility limit is about 3 times larger than that of a single crystal.

(2) The peak in dielectric constant due to a ferroelectric transition of $PbTiO_3$ shifted to lower temperature and finally could not observed with increasing Mg content. The dielectric loss increased in the sample which contained Mg^{2+} cations. These results strongly supports formation of the solid solutions.

(3) Dielectric loss measured in air is larger than that in Ar. This result indicates a defect structure in which Mg^{2+} enters B-site and, as a result, vacancies in A-site cation site and oxygen site is introduced.

References

1 J.P.Remeika and A.M.Glass, *Mater.Res.Bull.*, **5**, 37 (1970).

2 T.-Y.Tien and W.G.Carlson, *J.Amer.Ceram.Soc.*, **45**, 567 (1962).

3 M.Kobune, C.Sakamoto, S.Fujii and Y.Sugie, *J.Ceram.Soc.Jpn.*, **96**, 935 (1988).

4 Y.Takahashi, K.Niwa, K.Kobayashi and M.Matsuki, *J.Ceram.Soc.Jpn.*, **66**, 363 (1983).

5 G.Shirane and S.Hoshino, *J.Phys.Soc.Jpn.*, **6**, 265 (1951).

Chapter 2

Dielectric anomaly and ionic conduction in A-site deficient La-Ti-Al-O perovskites

2.1 Introduction

A number of titanates with perovskite structure have been developed for advanced dielectric materials such as $BaTiO_3$, $PbTiO_3$ and PLZT (Pb-La-Zr-Ti-O). Lanthanum titanate, $La_{2/3}TiO_3$, is expected to have a unique deficient perovskite-type structure with one-third of lanthanum sites (A-sites) vacant [1] and, therefore, to show unique electrical properties. However, pure $La_{2/3}TiO_3$ has not yet been prepared [2].

The perovskite structure has been stabilized by changing its chemical composition slightly. Abe and Uchino prepared $La_{2/3}TiO_{3-\delta}$ perovskites with oxygen vacancy, δ, ranging from 0.007 to 0.079 under reduced oxygen pressures and examined the crystallographic properties [3]. They reported that the compound is orthorhombic and has the superstructure with a doubled unit cell along the *c*-axis when δ is small. They also claimed that ordering of the cation vacancies on the A-sites is responsible for the superstructure; namely, the LaO(1) plane contains a small amount of cation vacancies and the LaO(2) plane contains a large amount of cation vacancies which are alternately sited up along the *c*-axis.

In the system $La_{2/3}TiO_3$-$SrTiO_3$, perovskite solid solutions were formed up to a composition of 94 mol% $La_{2/3}TiO_3$; moreover, the superstructure was observed at compositions containing more than 70 mol% of $La_{2/3}TiO_3$ [4]. Dielectric relaxation was observed for the system $La_{2/3}TiO_3$-$SrTiO_3$, but no detailed information was given [5]. As Sr^{2+} enters the A-site of the perovskite structure, the amount of A-site vacancies are reduced from 1/3 to 1/3-*x*/3 as shown in the eqn. (2.1), leading to the stabilization of the perovskite structure.

$$(1\text{-}x)\ La_{2/3}TiO_3 + x\ SrTiO_3 \rightarrow (La_{2/3\text{-}2x/3}Sr_x)TiO_3 \qquad (2.1)$$

Alkali metals such as Na and Li also stabilize the perovskite structure [6]. The

amount of A-site vacancies are reduced by filling them up with Na or Li. The compounds thus obtained are known to be good alkali metal ion conductors [7].

In this study, it has been found that the perovskite structure is also stabilized by partial substitution for Ti^{4+} with Al^{3+}. The stabilization was also found by Negas *et al.* [8] and Škapin *et al.* [9] In this system the A-site vacancies decreases from 1/3 to 1/3-*x*/3 by B-site substitution as shown in the eqn. (2.2).

$$(1\text{-}x)\ La_{2/3}TiO_3 + x\ LaAlO_3 \rightarrow La_{2/3+x/3}(Ti_{1-x}Al_x)O_3 \qquad (2.2)$$

A remarkable dielectric relaxation was observed for the La-Ti-Al-O perovskites when the Al content was small (x = 0.05 - 0.15). The dielectric relaxation was characterised by a maximum in dielectric loss and an increase in dielectric constant (relative permittivity) at low frequency.

In this chapter, systematic investigations of the dielectric and complex impedance measurements were performed on La-Ti-Al-O perovskites. This work demonstrates oxide ion conduction in the La-Ti-Al-O perovskites which is responsible for the dielectric relaxation. The oxide ion conduction in the A-site deficient perovskites is discussed in relation to the structural information obtained by the Rietveld analysis for the powder X-ray diffraction patterns.

2.2 Experimental

Sample preparation and characterization

All samples were prepared by solid state reactions of La_2O_3, TiO_2 and Al_2O_3 powders of purity > 99.9%. Compositions tested are shown in Table 2.1; samples with x ranging from 0 to 0.2 for $(1\text{-}x)La_{2/3}TiO_3$ - $xLaAlO_3$ were prepared. Starting powders were prefired at 1273 K for 4 h, weighed, and well ground with ethanol in an agate mortar.

The mixtures were calcined at 1623 or 1673 K for 8 h in a flowing N_2 - O_2 atmosphere and reground. Calcination and regrinding were repeated 4 - 8 times until no change in the powder X-ray diffraction patterns was observed. The calcined powders were pressed into pellets and sintered at 1623 or 1673 K for 8 h in a flowing O_2 atmosphere.

Phases in the samples were identified by X-ray powder diffraction analysis. Sintered

Table 2.1 Nominal compositions of the samples.

sample	x	$La_{2/3}TiO_3$	$LaAlO_3$	nominal composition
LT	0	1.0	0	$La_{0.6667}TiO_3$
LTA05	0.05	0.95	0.05	$La_{0.6833}Ti_{0.95}Al_{0.05}O_3$
LTA10	0.10	0.90	0.10	$La_{0.7000}Ti_{0.90}Al_{0.10}O_3$
LTA15	0.15	0.85	0.15	$La_{0.7167}Ti_{0.85}Al_{0.15}O_3$
LTA20	0.20	0.80	0.20	$La_{0.7333}Ti_{0.80}Al_{0.20}O_3$

densities were measured with immersion in water by the Archimedes method. A scanning electron microscope was used to observe the microstructures and measure the grain sizes.

Pellets of ZrO_2 stabilized with 15 mol% CaO (CSZ) were also prepared by a standard powder method. They were used to check the performance of electrical measurements.

Complex impedance and dielectric measurements

Prior to the measurements, both sides of the sample pellets were polished and, if needed, heat-treated in an atmosphere of O_2, Ar or air. After this, Pt - Pd electrodes were formed on both sides by sputtering. Dielectric constant, dielectric loss, absolute value of vector impedance, and phase angle were measured simultaneously by the two-terminal method using YHP 4274A and 4275A LCR meters with an applied voltage of 1 or 5 V, frequency range from 100 to 4 MHz, and temperature range from 293 to 1073 K. The results were reproducible for the heating cycles indicating that the oxidation state did not change. Thus, in general, we employed the same atmospheric conditions for measurements as that for the sintering or annealing.

EMF measurements with a gas concentration cell

The open circuit voltage on the sintered pellets with sputter-deposited electrodes was measured using a Keithley 617 digital meter in a gas concentration cell at 773-873 K. Oxygen partial pressures ranging from 0.1 to 0.9 were used for one side; atmospheric pressure was employed for the other side as a reference gas. Ionic transport number was calculated from the slope in the plot of the measured open circuit voltage *vs.* the oxygen partial pressure which

was compared with the theoretical value of the Nernst equation.

Rietveld analysis

Powder X-ray diffraction patterns for the Rietveld analysis were obtained by a step scanning method with a scanning interval of 0.04° using a rotating-anode type X-ray generator. The Rietveld analysis software, RIETAN, written by Izumi [10] were used to refine the precise structural parameters.

2.3 Results and Discussion

Complex impedance analysis

All sintered pellets were brownish white and their sintered densities were 95 -98% of theoretical. Microscopic observation by scanning electron microscopy revealed considerable grain growth; the average grain sizes were 5 -15 μm. X-ray diffraction patterns in the composition range x = 0.05 - 0.20 showed the presence of perovskite having a superstructure with a doubled c-axis parameter. Our phase identification was in good agreement with that reported by Škapin *et al.* [9] A trace of an impurity $La_2Ti_2O_7$ pyrochlore phase existed and its amount slightly increased in LTA20. It is noteworthy that the partial substitution stabilized the perovskite structure. In pure $La_{2/3}TiO_3$ composition (LT), no perovskite phase formed and a mixture of $La_2Ti_2O_7$ and $La_4Ti_9O_{24}$ was obtained.

Complex impedance results measured on LTA05 and LTA20 at 873 K are shown in Fig. 2.1. Two semicircles were observed in the Cole - Cole plots for both LTA05 and LTA20. Frequencies at maximum Z'' (the top of semicircles) and minimum Z'' (the neck between semicircles) are also shown. Note that the maximum of the low frequency semicircle for LTA05 was lower than the frequency we could measure with our LCR meter (100 Hz); for this reason, the maximum frequency was estimated by extrapolation. The higher frequency semicircle of LTA05 is very small compared with the lower frequency semicircle. In LTA20, two semicircles are similar in size; moreover, considerable overlap of two semicircles is observed.

It is known that two semicircles in an impedance plot are well explained by an equivalent circuit shown in Fig. 2.2. If we assume that R_1C_1 is less than R_2C_2, the parallel circuit consisting of R_1 and C_1 corresponds to the higher frequency semicircle; the R_2 and C_2

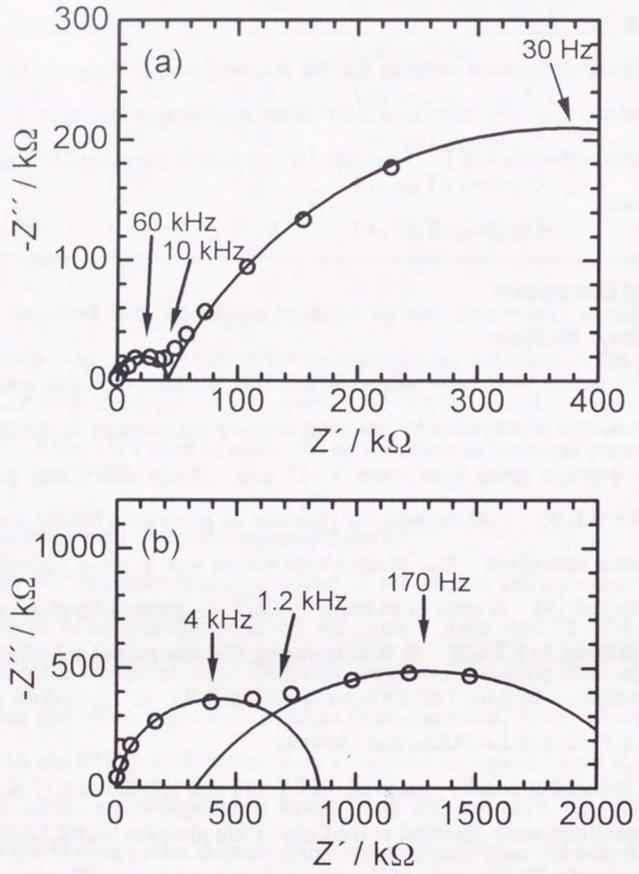

Fig. 2.1 Impedance plots of $La_{2/3+x/3}(Ti_{1-x}Al_x)O_3$ measured at 873 K. (a) $x = 0.05$ (LTA05) and (b) $x = 0.20$ (LTA20)

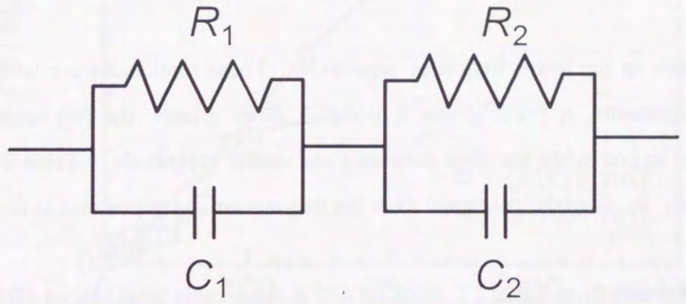

Fig. 2.2 Equivalent circuit used for $La_{2/3+x/3}(Ti_{1-x}Al_x)O_3$.

Table 2.2 Time constants and resistance and capacitance values of $La_{2/3+x/3}(Ti_{1-x}Al_x)O_3$ with $x = 0.05$(LTA05) and 0.20(LTA20). These parameters were calculated from the data plotted in Fig. 2.1 (a) and (b), assuming a parallel equivalent circuit as shown in Fig. 2.2.

sample	T / K	τ_1 / ms	τ_2 / ms	R_1 / kΩ	R_2 / kΩ	C_1 / pF	C_2 / nF
LTA05	873	0.017	33	42	740	400	45
LTA20	873	0.25	5.9	850	2340	310	2.5

circuit corresponds to the lower frequency semicircle. These semicircles are well separated when the time constants, τ_1 (=R_1C_1) and τ_2 (=R_2C_2), differ greatly; the two semicircles are considerably overlapped when the time constants are similar magnitude. Table 2.2 lists the values of τ_1, τ_2, R_1, R_2, C_1 and C_2 obtained from the frequencies and impedance at the top of the semicircles.

As can be seen from Table 2.2, R_1 of LTA05 is remarkably small, about 1/20 of that of LTA20. Also, C_2 of LTA05 is about 20 times larger than that of LTA20. Consequently, the time constants, τ_1 and τ_2, of LTA05 differ by more than 3 orders of magnitude decades, resulting in a clear separation of the semicircles. In contrast, the time constants of LTA20 differ by only 20, causing a large overlap of the semicircles.

Effects of sample thickness and measuring atmosphere on the impedance

Impedance plots for ceramic samples often give multiple semicircles as observed in Fig. 2.1. These semicircles are often referred to polarization in bulk grains, grain boundaries, and electrode interfaces in order of decreasing frequency. It is also known that the semicircle arising from grain boundaries or electrode interfaces is sometimes missing. Therefore, impedance measurements were performed with changing sample thickness in order to investigate what is responsible for each semicircle in the impedance plot of LTA shown in Fig. 2.1.

Figure 2.3 shows the impedance plots at 773 K for two LTA05 samples having different thickness; the thicker sample has approximately double the thickness and the same electrode area as the thinner one. The higher frequency semicircle of the thicker sample is doubled in size, suggesting that the polarization occurs in the bulk grains. Also, the size of the

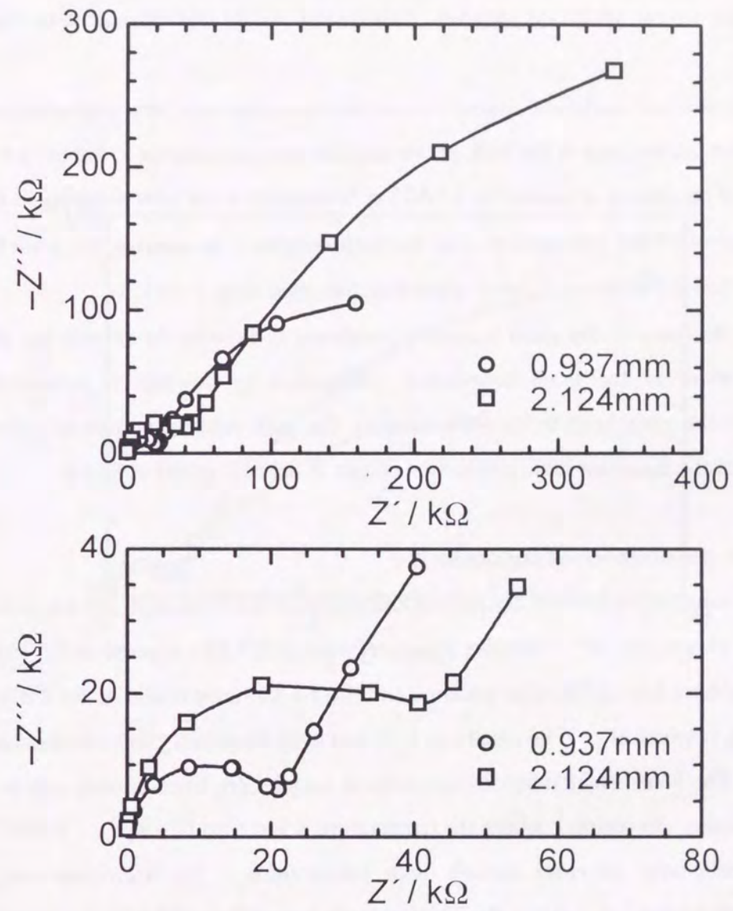

Fig. 2.3 Impedance plots for two $La_{0.6833}Ti_{0.95}Al_{0.05}O_3$ (LTA05) samples having different thickness of 0.937 mm (○) and 2.124 mm (□) measured at 773 K.

lower frequency semicircle changes in accordance with the sample thickness. This indicates that the lower frequency semicircles arise from polarization in the grain boundaries, since the semicircle due to the electrode interface polarization would not change with the sample thickness.

The effect of measuring atmosphere on the impedance was next evaluated to explore the conduction mechanisms in the bulk grains and the grain boundaries. Figure 2.4 shows a comparison of the measured results for LTA05 in flowing O_2 or Ar after sintering in O_2. The bulk resistance of 19 kΩ is almost the same for both samples. In contrast, the grain boundary resistance of 260 kΩ in O_2 is 1.5 times larger than the value in Ar (170 kΩ).

The decrease in the grain boundary resistance in flowing Ar reveals the electronic conductive nature of the grain boundaries. Reduction in flowing Ar enhanced *n*-type conduction in the grain boundaries. By contrast, the bulk resistance showed little change, suggesting that the dominant ionic conduction occurs in the bulk grains at 833 K.

Temperature dependence of conductivity

The temperature dependence of bulk and grain boundary conductivity was investigated in (*i*) O_2, (*ii*) air and (*iii*) Ar. Samples measured were (*i*) LTA05 sintered in O_2, (*ii*) LTA05 annealed in air for 1 h at 1273K after sintering and (*iii*) LTA05 annealed in Ar for 1 h at 1273 K after sintering, respectively. The results on bulk and grain boundary conductivities are shown in Fig. 2.5. The bulk conductivity for the sintered sample [(*i*), open circles] can be divided into three regions. In region I, where the temperature is less than 673 K (*i.e.*, $1000/T < 1.5$), the bulk conductivity increases linearly with temperature. The activation energy was calculated as 40 kJ mol^{-1} (0.4 eV). Region II extends from 673 to 873 K ($1.5 < 1000/T < 1.1$) with an activation energy of 30 kJ mol^{-1} (0.3 eV). In regions I and II, ionic conduction is believed to be dominant in the bulk grains, as discussed in the previous section. The observed low activation energies also suggest the dominant contribution of ionic conduction. The activation energy increases again in region III above 873 K.

Bulk conductivity in air [(*ii*), open squares] shows a similar temperature variation with slightly larger values than that in O_2. Also, the grain boundary conductivity is similar for measurements in air and in O_2. As a whole, the electrical properties of LTA05 are very similar in air and in O_2 ; both bulk and grain boundary conductivities were enhanced with the sample

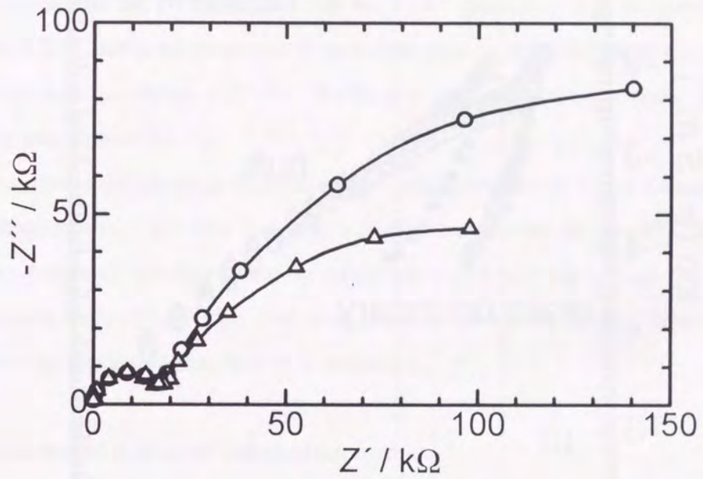

Fig. 2.4 Impedance plots of $La_{0.6833}Ti_{0.95}Al_{0.05}O_3$ (LTA05) measured in O_2 (○) and Ar (△) at 833 K after sintering in O_2.

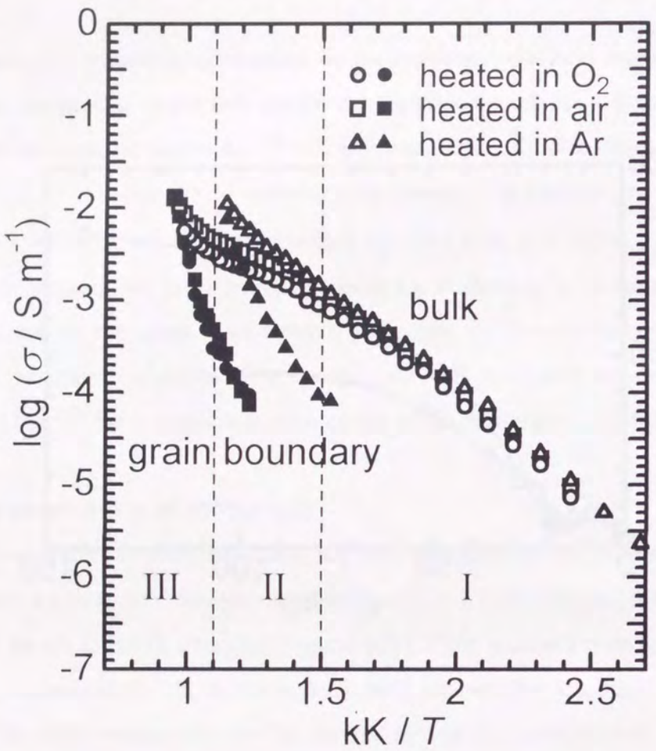

Fig. 2.5 Temperature dependence of bulk and grain boundary conductivities for $La_{0.6833}Ti_{0.95}Al_{0.05}O_3$ (LTA05) heated in various atmosphere: heated in O_2 (○, ●), air (□, ■) and Ar (△, ▲) for bulk (open symbols) and grain boundary (filled symbols).

reduction in air at high temperature similarly as in O_2.

The Ar-annealed sample [(*iii*), open triangles] shows a basically identical bulk conductivity with those annealed in air and O_2 in region I below 673 K. However, it differs in terms of the temperature dependence above 673 K; the activation energy continuously increases in region II with no intermediate reduced activation energy. It is also noticed that the grain boundary conductivity (filled triangles) starts to increase at much lower temperature than for samples in air and in O_2. This reveals that the bulk conduction in an Ar-annealed sample is ionic below 673 K, while an electronic contribution may be present both in the bulk and grain boundary conduction above 673 K. Reduction proceeds into the bulk grain on high temperature annealing in Ar.

Figure 2.6 shows the temperature variations of bulk conductivity of LTA sintered in O_2 with various compositions. LTA05 has the highest conductivity below 873 K. The bulk conductivity decreases with increasing the Al content to LTA10 and LTA15. LTA20 has one tenth the conductivity of LTA15. The conductivities are similar among these samples above 873 K where the electronic contribution is dominant.

EMF measurement and ionic conduction species

Ionic conduction is assumed to be dominant below 873 K in the samples heated in air or in O_2 in the above discussion. EMF measurements were performed on LTA05 using an oxygen gas concentration cell to evaluate ionic transport number, t. Open circuit voltage was measured on the concentration cell against air as a reference electrode. It continuously changed with oxygen concentration in an N_2 - O_2 mixture on the measuring electrode. This phenomenon supports that bulk ionic conduction occurs in LTA05. Table 3.3 lists ionic transport numbers at various temperatures. At 773 K this is very close to a unity showing

Table 2.3 Ionic transport number of $La_{0.6833}Ti_{0.95}Al_{0.05}O_3$ (LTA05).

T / K	t
773	0.99
823	0.91
873	0.62

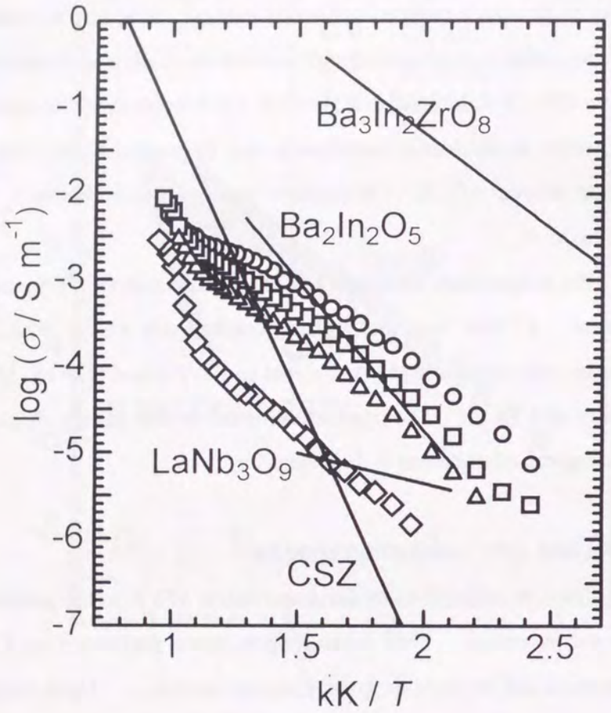

Fig. 2.6 Temperature dependence of bulk conductivity of $La_{2/3+x/3}(Ti_{1-x}Al_x)O_3$ with various compositions sintered in O_2: x = 0.05 (LTA05,○), 0.1 (LTA10,□), 0.15 (LTA15,△) and 0.20 (LTA20,◇). Oxide ion conductivity of various compounds is also shown for comparison.

almost pure ionic conduction; above this temperature an increased electronic contribution reduced the ionic transport number.

The appearance of an open circuit voltage does not necessarily mean that the mobile species is oxide ion. Nevertheless, it is reasonable to consider the oxide ion conduction since ionic conduction of trivalent or quadrivalent cations has not been so far satisfactorily demonstrated except for the trivalent cation conductors, $Al_2(WO_4)_3$ [11] and $Sc_2(WO_4)_3$ [12]. Direct experimental determination of oxide ion conduction using the oxygen gas pumping method, however, could not be applied to LTA because of increasing electronic conduction at high temperature and insufficient ionic conductivity for the low temperature operation.

To confirm the oxide ion conduction, we investigated a change in the terminal voltage by connecting external resistance to the gas concentration cell. The terminal voltage decreased by two-thirds on connecting a 10 MΩ resistance; however, a stable voltage was observed over 30 h. This results indicate that the electrical current could be drawn stably from the concentration cell and thus indicate dominant oxide ion conduction. The decrease in the terminal voltage is probably due to insufficient ionic conductivity and large grain boundary resistance.

It is noteworthy that the conductivity of LTA05 at 773 K did not vary from flowing air to flowing dry N_2. This indicates that the contribution of the proton conduction is small in LTA05, in contrast to proton conducting *p*-type perovskite oxides.

Dielectric relaxation

LTA05 showed remarkable dielectric relaxation which is characterized by a maximum in dielectric loss *vs.* frequency and an increase in dielectric constant with decreasing frequency. With an increase in the Al content the maximum in dielectric loss showed a remarkable broadening. Finally, a maximum was no longer observed for LTA20; only a slight increase was observed at around 1 kHz.

Comparison of the dielectric and impedance measurements revealed that the frequencies at the neck in Fig. 2.1 directly correspond to the frequencies of the dielectric loss maxima. This correspondence can be understood from the following relation;

$$\tan \delta = 1 / \tan \theta = |Z'| / |Z''| \qquad (2.3)$$

where θ is the impedance phase angle. This equation means that the dielectric loss of LTA05

shows a pronounced maximum because | Z'' | is small enough at the neck. Because of the large overlap of the semicircles, | Z'' | of LTA20 is not so small at the neck, corresponding to the only slight increase in the dielectric loss.

As observed in Table 2.1, the clear separation of the semicircles on LTA05 is ascribed to the small R_1 (bulk grain resistance) and large C_2 (grain boundary capacitance). Moreover, at this temperature, bulk grain conductivity is dominated by oxide ion conduction. Thus it is concluded that the dielectric relaxation in LTA05 is attributed to the high oxide ion conductivity in the bulk grain and a high capacitance value in the grain boundary.

Rietveld analysis

X-ray diffraction patterns of LTA showed superstructure diffraction lines of a doubled lattice parameter along the *c*-axis similarly to $La_{2/3}TiO_{3-\delta}$ [3]. Rietveld refinement was started from a structure model shown in Fig. 2.7. Two types of LaO plane are alternately built up; LaO(1) and LaO(2) planes have a small and large amounts of La vacancies, respectively. Ti^{4+} and Al^{3+} are randomly distributed on the B-sites. The space group was assumed to be orthorhombic *P/mmm* for LTA05 and LTA10 since there are 200, 020 and 002 diffraction peaks. LTA15 and LTA20 have tetragonal *P4/mmm* lattices. Isotropic thermal parameters were used for all constituent ions to converge the preliminary refinement. A common thermal parameter was applied to all oxide ions.

The crystal structure could be refined to reasonable values as shown in Table 2.4. Figure 2.8 shows the variation of the lattice parameters and a cube root of the cell volume *vs.* Al content, *x*. LTA20 is very close to a cubic perovskite structure except for the existence of cation vacancy ordering. The cell volume of LTA increases linearly with decreasing *x*. The expansion of 0.3 % from LTA20 to LTA05 is mainly due to the difference in the ionic radii between Ti^{4+} (0.0605 nm) and Al^{3+}(0.0530 nm) [13]. A marked increase in the *c*-axis parameter with decreasing *x*, however, is noted; the lattice expansion along the *c*-axis is 0.7%. The *c*-axis expansion is closely related to the cation vacancy ordering discussed below.

The occupation factors of La in the LaO planes are shown in Fig. 2.9. It reveals that almost all A-site vacancies of LTA05 and LTA10 are distributed in the LaO(2) plane. A decrease in the LaO(1) occupation factor together with an increase in LaO(2) make LTA20 close to an ordinary cubic perovskite structure, as is also seen from the lattice parameter

Table 2.4 Experimental conditions and results of the Rietveld analysis on $La_{2/3-x/3}(Ti_{1-x}Al_x)O_3$.

x		0.05	0.10	0.15	0.20
Radiation		CuKα	CuKα	CuKα	CuKα
Range 2θ/°		10-130	10-130	10-130	10-130
Step width		0.04	0.04	0.04	0.04
Crystal system		orthorhombic	orthorhombic	tetragonal	tetragonal
Space group		*P/mmm*	*P/mmm*	*P4/mmm*	*P4/mmm*
Reliable Factor	R_{wp} (%)	16.78	15.31	17.96	18.38
	R_p (%)	12.29	11.16	13.68	13.98
	R_I (%)	6.10	5.26	7.78	9.05
	R_f (%)	3.85	3.57	5.26	6.84
Lattice parameter	*a*/nm	0.38589(1)	0.38587(1)	0.38625(1)	0.38612(4)
	b/nm	0.38704(1)	0.38673(1)	0.38625	0.38612
	c/nm	0.77754(2)	0.77581(2)	0.77372(3)	0.77228(15)
Occupation factor	La(1)	0.969(7)	0.966(6)	0.943(10)	0.867(12)
	La(2)	0.398	0.434	0.490	0.600
Position, *z*	Ti,Al	0.262(1)	0.261(1)	0.259(3)	0.258(4)
	O(1)	0.242(8)	0.241(10)	0.236(4)	0.241(6)
	O(2)	0.240(9)	0.231(10)	0.236	0.241
Thermal Parameter,	La(1)	0.44(10)	0.45(9)	0.35(15)	0.26(25)
B / $10^{-2}nm^2$	La(2)	0.54(22)	0.38(18)	0.09(27)	0.16(33)
	Ti,Al	0.43(14)	0.44(13)	0.37(20)	0.17(24)
	O	2.09(40)	1.44(29)	0.87(41)	1.16(49)

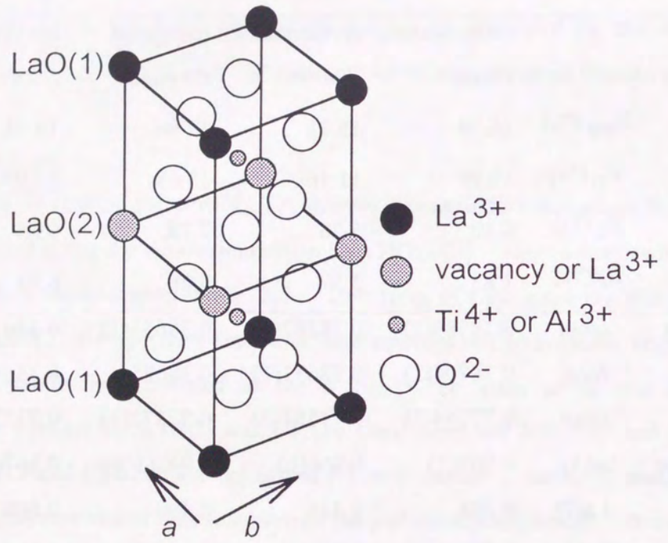

Fig. 2.7 Structure model of $La_{2/3+x/3}(Ti_{1-x}Al_x)O_3$ perovskites used for the Rietveld analysis.

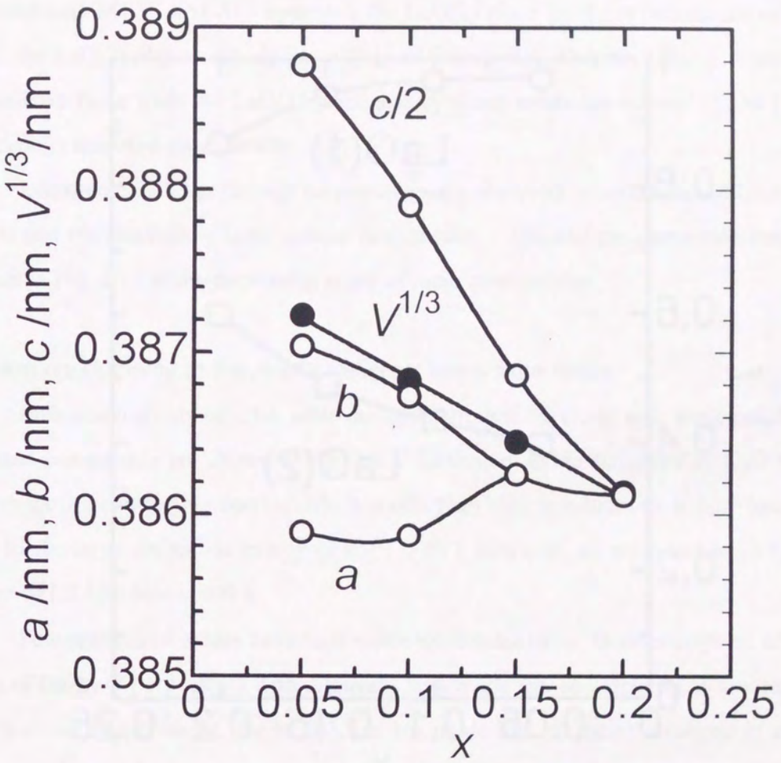

Fig. 2.8 Lattice parameters *versus* composition of $La_{2/3+x/3}(Ti_{1-x}Al_x)O_3$.

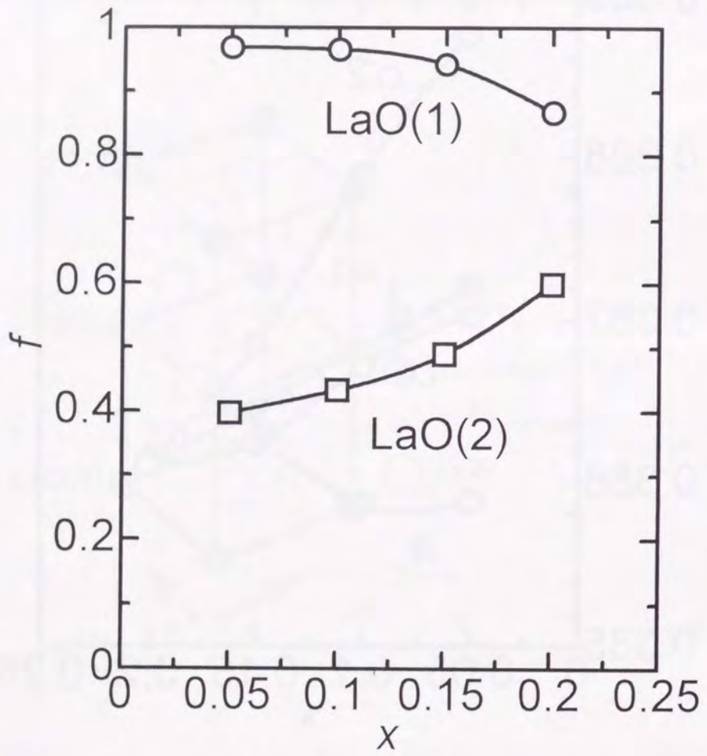

Fig. 2.9 La^{3+} occupation factors in LaO(1) and LaO(2) planes *versus* composition of $La_{2/3+x/3}(Ti_{1-x}Al_x)O_3$.

variation in Fig. 2.8.

The ionic displacements of LTA05 are shown in Fig. 2.10. As a result of the cation vacancy ordering, the LaO(1) plane has a positive charge and the LaO(2) has a negative charge. The B-site ions of Ti^{4+} and Al^{3+} approach the LaO(2) plane by 9 pm because of an attractive force to the LaO(2) plane. Oxide ions O(1) and O(2) in the $(Ti,Al)O_2$ plane lie 8 pm apart due to a repulsive force from the LaO(2) plane and by direct oxide ion contact. The (Ti, Al)-O_6 octahedron is distorted considerably.

Unexpectedly large thermal parameters were observed on oxide ions in LTA05. This suggests that the conducting ionic species is oxide ion. Thermal parameters decreased with x as shown in Fig. 2.11 in the decreasing order of ionic conductivity.

Oxide ion conductivity in the A-site deficient perovskite oxide

Bulk conductivity of LTA with various compositions along with ionic conductivity of the related compounds are shown in Fig. 2.6. Zirconium oxide stabilized by CaO (CSZ) is a typical oxide ion conducting ceramic which shows high ionic conductivity at high temperatures. Owing to the large activation energy (0.8 - 1.0 eV), however, its ionic conductivity is lower than that of LTA05 below 800 K.

Few perovskite oxides have high oxide ion conductivity; Goodenough *et. al.* prepared a series of Ba-In-O perovskites with relatively high oxide ion conductivity at low temperature [14]. Barium indium oxide ($Ba_2In_2O_5$) has 1/6 oxide ion vacancies arranged in an ordered manner. The activation energy of 0.74 eV is somewhat larger than of LTA05; the conductivity at 700 K is comparable to LTA05. Disordered oxide ion vacancies in $Ba_3In_2ZrO_8$ leads to much higher oxide ion conductivity as shown in Fig. 2.6; the activation energy is also lowered to 0.6 eV which is identical to that of LTA05. The disadvantage of these Ba-In-O perovskites is *p*-type electronic conduction in air with the ionic transport number being 0.93 - 0.96 at 773 K.

Lanthanum niobate ($LaNb_3O_9$) is a perovskite oxide with a large number of A-site vacancies. It has been reported to be a La ion conductor with fairly low conductivity and an extremely small activation energy of 0.19 eV [15]. The structure of $LaNb_3O_9$ resembles that of LTA05 having a superstructure with a doubled unit cell along the *c*-axis with two-thirds of the La site vacant. Oxide ions may also contribute to the conduction in $LaNb_3O_9$.

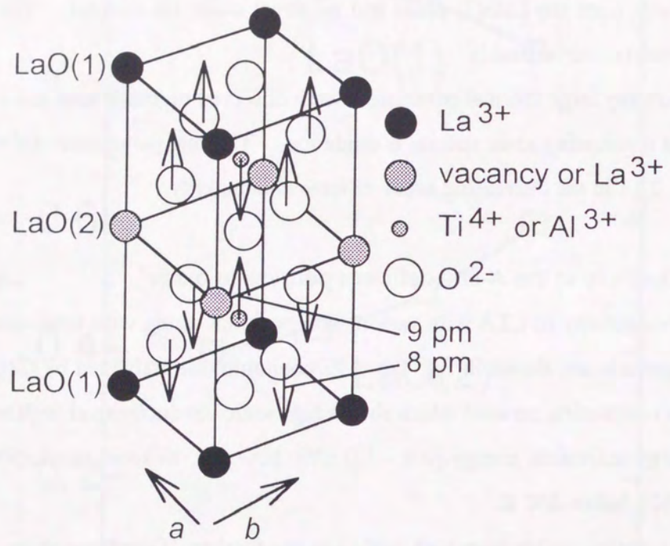

Fig. 2.10 Ionic displacements in $La_{2/3+x/3}(Ti_{1-x}Al_x)O_3$ refined by the Rietveld analysis.

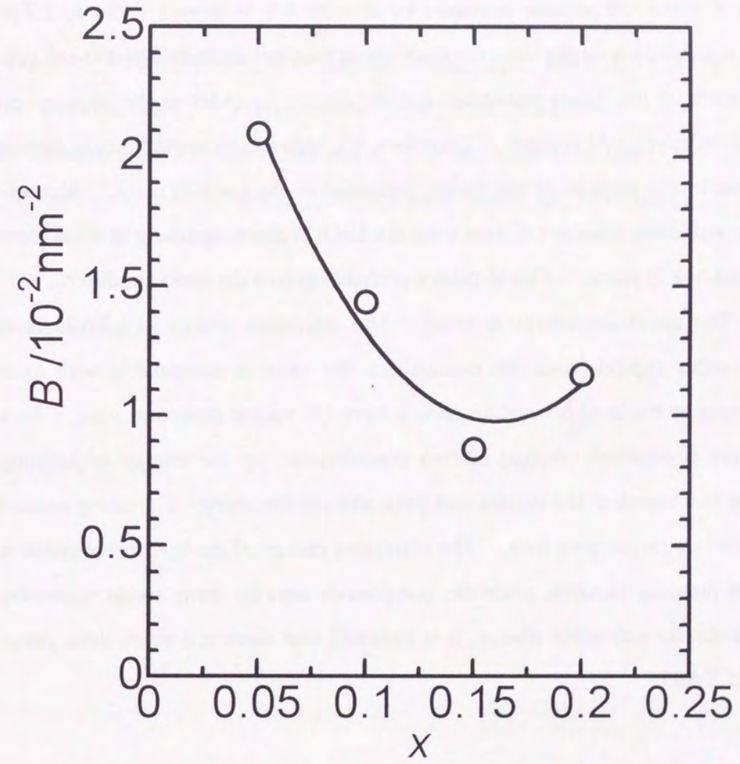

Fig. 2.11 Oxide ion thermal parameter *versus* composition of $La_{2/3+x/3}(Ti_{1-x}Al_x)O_3$.

As is distinct from other oxide ion conductors, the ionic conduction in LTA has the unique characteristics.

(*i*) LTA shows high ionic conductivity when the Al content is small. An increase in the cell volume with decreasing Al content may contribute to the enhancement of the ionic conductivity, but the cell volume increases by at most 0.3 % from LTA20 to LTA05. The effect of the composition on the ionic conductivity is thus not explained by the cell volume only. Both the amount of the A-site vacancies and the degree of order in the vacancy distribution increase with decreasing Al content. Therefore, the high ionic conductivity is strongly related to the increase in the amount of the cation vacancies in the LaO(2) plane. Moreover, oxide ions in upper and lower sides are distant from the LaO(2) plane, resulting in a low density in the vicinity of the LaO(2) plane. This structure probably favors the ionic condition.

(*ii*) The activation energy is small. The activation energy of LTA05 is very small compared to other typical oxide ion conductors; the value is comparable with or somewhat lower than those of Ba-In-O perovskites which have 1/6 vacant oxide ion sites. An activation energy of ionic conduction consists of two contribution: (*a*) the energy of jumping barriers existing in the bottleneck of the conduction pass, and (*b*) the energy of creating vacancies in the neighboring site of the jumping ions. The activation energy of Ba-In-O perovskites is equal to the energy of jumping barriers, since the compounds contain many oxide vacancies. Since LTA05 has a similar activation energy, it is assumed that there are many ionic jump sites for oxide ions in LTA05.

References

1 M. Kestigian and R. Ward, *J. Am. Chem. Soc.*, **76**, 6027 (1954).

2 J. B. MacChesney and H. A. Sauer, *J. Am. Ceram. Soc.*, **45**, 416 (1962).

3 M. Abe and K. Uchino, *Mater. Res. Bull.*, **9**, 147 (1974).

4 T. Y. Tien and F. A. Hummel, *Trans. Brit. Ceram Soc.*, **66**, 233 (1967).

5 J. Kainz, *Ber. Deut. Keram. Ges.*, **35**, 69 (1958).

6 A. G. Belous, G. N. Novitskaya, S. V. Polyanetsukaya and Yu. I. Gornikov, *Izv. Akad. Nauk SSSR, Neorg. Mater.*, **12**, 470 (1987).

7 Y. Inaguma, C. Liquan, M. Itoh, T. Nakamura, T. Uchida, H. Ikuta and M. Wakihara, *Solid State Commun.*, **86**, 689 (1993).

8 T. Negas, G. Yeager, S. Bell and R. Amren, *NIST Spec. Publ.*, **804**, 21 (1991).

9 S. Škapin, D. Kolar and D. Suvorov, *J. Am. Ceram. Soc.*, **76**, 2359 (1993).

10 F. Izumi, *Nippon Kessyou Gakkaishi*, **27**, 23 (1985).

11 Y. Kobayashi, T. Egawa, S. Tamura, N. Imanaka and G. Adachi, *Chem. Mater.*, **9**, 1649 (1997).

12 N. Imanaka, Y. Kobayashi and G. Adachi, *Chem., Lett.*, **1995**, 433 (1995).

13 R. D. Shannon and C. T. Prewiitt, *Acta Cryst.*, **B25**, 925 (1969).

14 J. B. Goodenough, J.E. Ruiz-Diaz and Y. S. Zhen, *Solid State Ionics*, **44**, 21 (1990).

15 A. M. George and A. N. Virkar, *J. Phys. Chem. Solids*, **49**, 743 (1988).

Chapter 3

Sol-gel preparation and defect structures of thin films in $PbTiO_3$-$La_{2/3}TiO_3$ solid solution

3.1 Introduction

Thin films of $PbTiO_3$-based solid solutions have been studied for various applications such as multilayer capacitors, electrostrictive actuators, and piezoelectric transducers. Solid solutions in the system $PbTiO_3$-$La_{2/3}TiO_3$ (PT-LT) is of interest not only from the practical use but from the standpoint of the stability of cation deficient perovskite structures.

In an equilibrium phase diagram of the system PbO-$LaO_{1.5}$-TiO_2, La can substitute for Pb in the perovskite phase of $PbTiO_3$ to form $Pb_{1-x}La_{2x/3}TiO_3$ with x up to 0.855 [1]. As x exceeds 0.855, $La_2Ti_2O_7$ is formed in addition to the perovskite phase and, for the composition of x = 1.0, $La_{2/3}TiO_3$ perovskite has not yet been prepared. Another equilibrium phase diagram displays that no compound with a perovskite structure is found in the system La_2O_3-TiO_2 [2]. Therefore the preparations of perovskite phases in the system La-Ti-O were studied by using La metal and sintering in vacuuo [3], sintering at reduced atmosphere [4], and an addition of a small amount of Sr [5]. Since these specimens contain Ti^{3+} or the dopant, pure $La_{2/3}TiO_3$ perovskite with Ti^{4+} have not been obtained.

In the previous chapter, it was shown that Al addition stabilizes the perovskite structure. Dielectric relaxation and oxide ion conduction of the La-Ti-Al-O perovskite were discussed in relation with the oxide ion vacancy ordering. In this chapter, thin films of PT-LT solid solutions with a wide range of composition are prepared by the sol-gel and dip-coating methods. The effectiveness for the preparation and the characteristics of the defect structure in the sol-gel method are discussed from structural analysis and electrical properties.

3.2 Experimental

A flow chart of the sol-gel preparation for PT-LT thin films is shown in Fig. 3.1 and nominal compositions for the stock solutions are shown in Table 3.1. Titanium tetra-isopropoxide (TIP) diluted with ethanol was used as a Ti source. Triethanolamine (TEA) was added to depress the hydrolysis and enhance the solubility of the acetate and nitrate [6]. A molar ratio of TEA to TIP was 1 for $x \leq 0.6$, and 2 for $x > 0.6$. The solution was partially hydrolyzed by 1:1 mixture of H_2O and ethanol. Prescribed amounts of lead (II) acetate ($Pb(OCOCH_3)_2 \cdot 3H_2O$) and lanthanum (III) nitrate ($La(NO_3)_3 \cdot 6H_2O$) previously dissolved in H_2O-ethanol were added to the solution and stirred vigorously. The clear stock solution was obtained and used for coating.

Table 3.1 Nominal compositions of the stock solution for $(1-x)PbTiO_3$-$xLa_{2/3}TiO_3$ films.

x	(TIP	EtOH	TEA)	(PbAC	LaNT)
0	1	8	1	1	0
0.1	1	8	1	0.9	0.07
0.2	1	8	1	0.8	0.13
0.3	1	8	1	0.7	0.20
0.4	1	8	1	0.6	0.27
0.5	1	8	1	0.5	0.33
0.6	1	8	1	0.4	0.40
0.8	1	8	2	0.2	0.53
0.9	1	8	2	0.1	0.60
0.95	1	8	2	0.05	0.63
1	1	8	2	0	0.67

TIP: titanium tetra-isopropoxide, TEA: triethanolamine
PbAC: lead (II) acetate, LaNT: lanthanum (III) nitrate

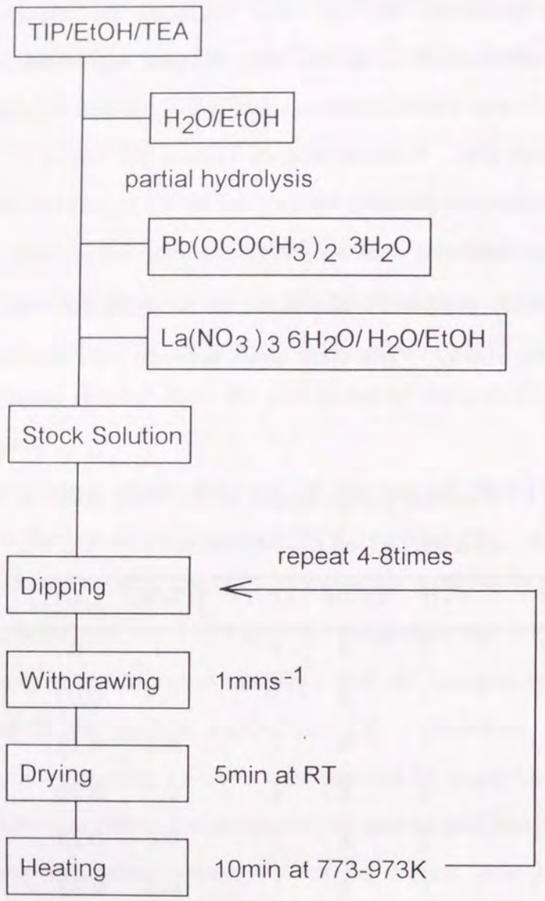

Fig. 3.1 Flow chart of the preparation for thin films of $PbTiO_3$-$La_{2/3}TiO_3$ solid solutions.

Substrates of slide glasses, quartz glasses, and platinum plates were dipped in the solution and withdrawn at a constant speed of 1 mm s^{-1}. The substrates were dried at room temperature for 5 min and heated at constant temperatures ranging from 773 K to 973 K for 10 min. The cycle of dipping, withdrawing, drying and heating was repeated 4 to 8 times, resulting in a film thickness of about 0.5 to 1.5 μm.

Phases present in the deposited and post heat-treated films were identified by X-ray diffraction analysis (XRD) with Cu Kα radiation. Lattice parameters were calculated by a least square method from the peak positions which were obtained by XRD step-scanning measurements and calibrated using Si powder as a standard. Compositions of the films were determined by an X-ray energy dispersion analyzer previously calibrated by calcined powder specimens of PbO, La_2O_3, and TiO_2 mixtures. Simulation of the XRD patterns were performed according to the defect structure model of the solid solutions using the Rietveld analysis software, RIETAN, made by Izumi [7]. Electrical properties were investigated for the films dipped on Pt substrates. Complex impedance between the Pt substrate and a sputtered Pt electrode on the film was measured using a YHP4274A LCR meter with frequencies of 100 - 100 kHz and applied voltage of 0.1 V.

3.3 Results

Phases in the Films

Figure 3.2 shows the relation between the nominal composition of the stock solutions and the measured composition of the deposited films. The composition in the films slightly deviated from the nominal composition; the ratio of Pb/Ti decreased linearly from 0.9 to 0, and the ratio of La/Ti increased from 0 to 0.6. This deviation demonstrates the difficulty of the sol-gel and dip-coating preparation for thin films with the desired composition. Note that precise discussion concerning the composition is limited, though the nominal composition is used for representing the composition of the films to avoid the complexity in the following description.

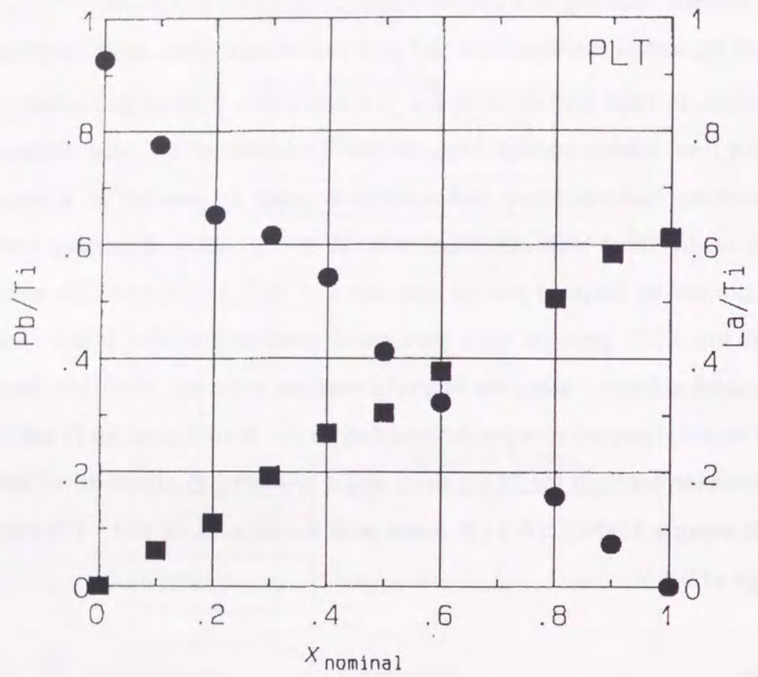

Fig. 3.2 Measured molar ratios of Pb/Ti and La/Ti in the sol-gel derived films of $PbTiO_3$-$La_{2/3}TiO_3$ as a function of the nominal composition of the stock solution.

XRD patterns of the PT-LT films, $(1-x)PbTiO_3$-$xLa_{2/3}TiO_3$ with $0 \leq x \leq 0.6$, deposited on slide glass substrates at 773 K are shown in Fig. 3.3. Halo patterns observed for (d) and (e) are ascribed to the scattering from slide glass substrates since the films deposited in (d) and (e) were thin. As can be seen from the peak separation such as 001 and 100, 110 and 101 in (a), the perovskite phase formed in the films of $x = 0$ have a tetragonal symmetry. The separation becomes small for $x = 0.1$, and cubic perovskite phases are obtained for $0.3 \leq x \leq 0.5$. Amorphous phase was obtained for $x = 0.6$ and crystallized to cubic after the post heat treatment at 823 K for 1 h.

With the composition $x \geq 0.8$, black films due to the residual carbon were formed by the deposition at 773 K. Thus heating in the dip-coating process for the composition $x \geq 0.8$ were conducted at 973 K using quartz glass substrates. Amorphous films were formed for the composition $0.8 \leq x \leq 1.0$ even by the heating temperature as high as 973 K. XRD patterns of the films after the post heat treatments at 1073 K for 1 h are shown in Fig. 3.4. Most of diffraction peaks from the cubic perovskite phase such as 110, 111, 200 and 211 were observed up to $x = 1.0$, though the intensity ratio varied with composition, which was obvious for 100 and 210 peak intensity. Small peaks appeared at $2\theta \sim 28°$ and 30° for $x = 0.95$ and were evident for $x = 1.0$. This second phase could be identified as pyrochlore-type $La_2Ti_2O_7$ from the peak positions.

Lattice Parameters

Lattice parameters of the perovskite phases are shown in Fig. 3.5 as a function of the composition. Comparison of the measured lattice parameters for the tetragonal phases of $x = 0$ with the published values for a single crystal [8] and with that of the sol-gel derived powder presented in chapter 1 shows that a-axis in the film is slightly large and c-axis is slightly small, resulting in a decrease in tetragonality, c/a, of the perovskite phase from 1.064 for the single crystal and 1.061 for the sol-gel derived powder to 1.044 for the sol-gel derived film. The tetragonality decreased with the composition as 1.013 for $x = 0.1$, and very close to unity for $x = 0.2$, no longer

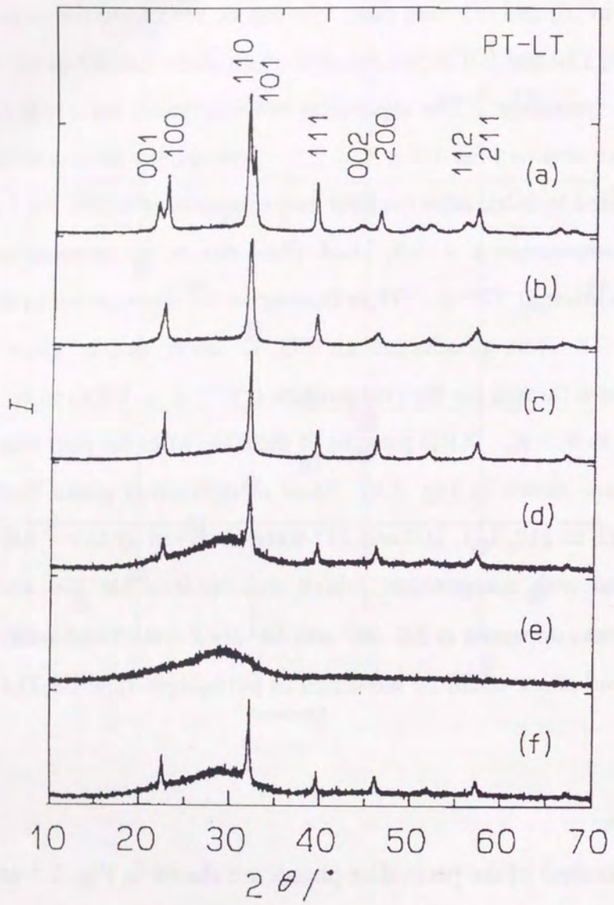

Fig. 3.3 X-ray diffraction patterns of the thin films for (1-x)$PbTiO_3$-$xLa_{2/3}TiO_3$. (a) $x = 0$, (b) $x = 0.1$, (c) $x = 0.3$, (d) $x = 0.5$, (e) $x = 0.6$ (as-deposited), and (f) $x = 0.6$ (heat-treated at 823 K for 1 h).

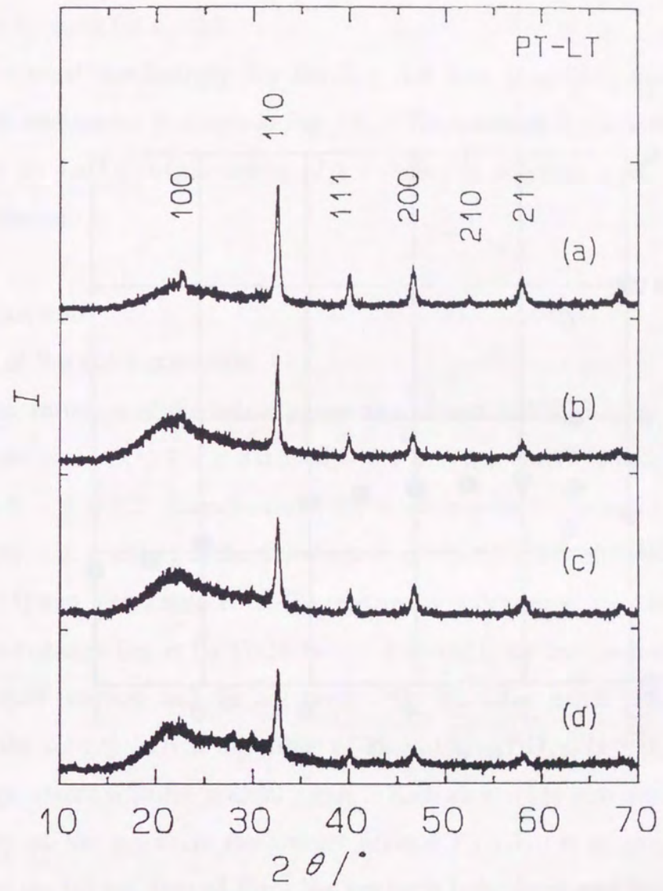

Fig. 3.4 X-ray diffraction patterns of the thin films for (1-x)$PbTiO_3$-$xLa_{2/3}TiO_3$ after the post heat treatment at 1073 K for 1 h. (a) $x = 0.8$, (b) $x = 0.9$, (c) $x = 0.95$, and (d) $x = 1.0$.

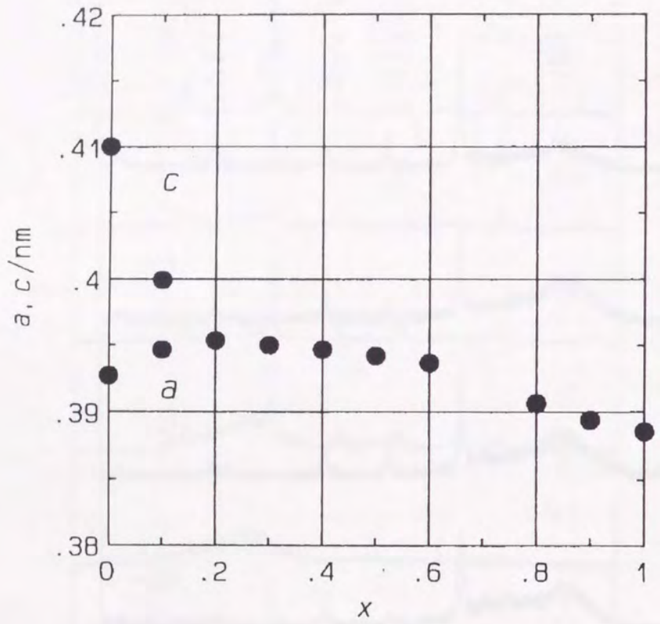

Fig. 3.5 Lattice parameters of the thin films for (1-x)$PbTiO_3$-$xLa_{2/3}TiO_3$ as a function of the composition.

distinguishable with the cubic phase. Thus we calculated the lattice parameters as a cubic structure in the case for $x \geq 0.2$. The lattice parameters of the cubic phases decreased with an increase in x gradually up to $x = 0.6$, then rapidly for $0.6 < x \leq 0.9$, and gradually again for $x > 0.9$.

Electrical conductivity for the $x = 1.0$ film ($La_{2/3}TiO_3$ composition) as a function of temperature is shown in Fig. 3.6. The conductivity is fairly low compared with those for La-Ti-Al-O ceramics of $x = 0.05$ - 0.20 which were described in the previous chapter.

3.4 Discussion

Structure of the solid solutions

The variation of the lattice parameters shown in Fig. 3.5 can be divided into three regions, that is, (1) $0 \leq x \leq 0.2$, (2) $0.2 \leq x \leq 0.6$, and (3) $0.8 \leq x \leq 1.0$. In the region (1) $0 \leq x \leq 0.2$, formation of solid solution with La caused a decrease in the tetragonality, c/a, resulting in the transformation into the cubic phase at $x = 0.2$. Both Hennings [1] and Yamamoto *et al.* [9] reported that the phase boundary of tetragonal and cubic structures lies at La 27-28 % ($x = 0.41$-0.42) for the specimens prepared by the solid state reaction and the hot press. On the other hand, Shimizu *et al.* [10] identified the sol-gel derived thin films of $Pb_{0.755}La_{0.188}TiO_{3.04}$ ($x = 0.245$) as pseudo-cubic in agreement with the present result. Kani *et al.* [11] also mentioned the poor crystallinity of the grains in the sol-gel derived PT-LT. It is considered that the structure of the sol-gel derived films has not been fully developed because of the low heating temperature, resulting in the shift of the phase boundary to about $x = 0.2$.

The lattice parameters in the region (2) $0.2 \leq x \leq 0.6$ decreased linearly with the composition. The decrease in this region represents a change in the cubic cell lattice parameters with an increase in the La content. Thus the decrease is ascribed to the difference between the ionic radii of Pb^{2+} (0.149 nm) and La^{3+} (0.132 nm) [12] and the formation of cation vacancies.

In the region (3) $0.8 \leq x \leq 1.0$, the change of lattice parameters becomes

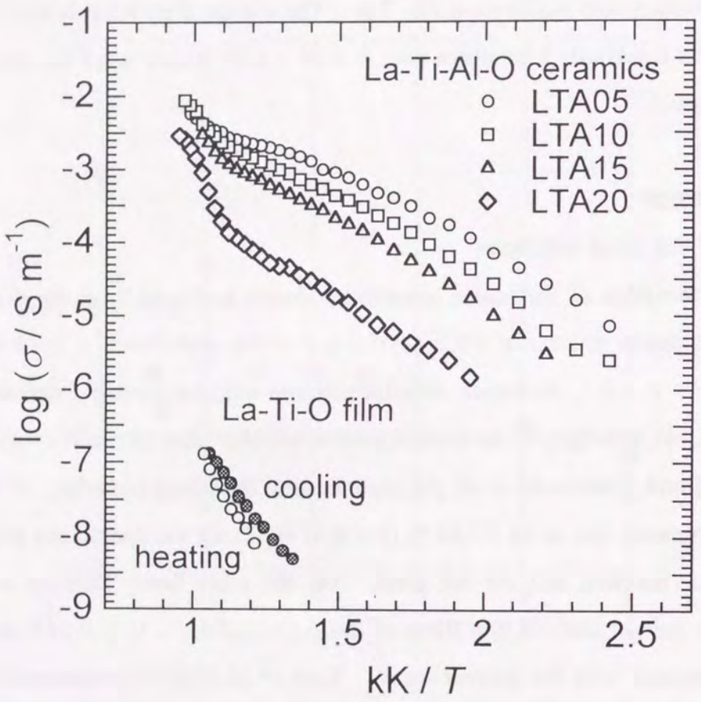

Fig. 3.6 Comparison of the electrical conductivity of the sol-gel derived La-Ti-O films and La-Ti-Al-O ceramics.

gradually with $x \geq 0.95$, corresponding to the appearance of the peaks from the second phase as shown in Fig. 3.4 (c) and (d). Thus the solubility limit of LT in PT is determined near $x = 0.90$, almost identical with the value, $x = 0.855$, obtained from the equilibrium phase diagram [1]. The enhancement of the solubility limit by the sol-gel method was not clearly seen in the present system as is distinct from the $(1-x)PbTiO_3$-$xMgTiO_3$ discussed in chapter 1, where the solubility limit increases by 3 times than the single crystal. This suggests that the sol-gel preparation expands the solubility limit more effectively for the system which hardly form a solid solution in a stable state.

Perovskite phase in La-Ti-O

A cubic perovskite phase with a small amount of the impurity pyrochlore phase, $La_2Ti_2O_7$, is formed at the composition $x = 1.0$ (corresponding to $La_{2/3}TiO_3$) as shown in Fig. 3.4(d). No perovskite phase, however, appeared in an equilibrium phase diagram of $LaO_{1.5}$-TiO_2 [4]. The fact that $La_{2/3}TiO_3$ is not available as a stable phase indicates the stability limit of A-site cation deficiency in the perovskite structure. The obtained perovskite phase in this study is considered to be metastable and actually decomposed to $La_2Ti_2O_7$ and $La_4Ti_9O_{24}$ by a heat treatment at a higher temperature of 1273 K.

Prasadarao *et al.* [13] have investigated a perovskite phase as an intermediate phase in the course of preparing $La_2Ti_2O_7$ from alkoxide precursors. The cubic perovskite phase was formed on heating at 1073 K and $La_2Ti_2O_7$ began to appear on heating at higher temperatures. This metastable phase is basically identical to the perovskite phase obtained in the present study. However, they did not characterize the perovskite phase except the lattice constant of 0.391 nm. Moreover, composition of the whole sample (La/Ti = 1) was somewhat different from $La_{2/3}TiO_3$.

Abe and Uchino [4] prepared the specimens of $La_{2/3}TiO_{3-\delta}$ perovskites from oxide mixtures in the reduced atmosphere. The structures of their specimens differ from that in the present study because they probably have Ti^{3+} and the oxygen defect.

Also, superlattice lines were observed, indicating the ordering of the cation vacancy formed during heat treatments at high temperatures which are required for the completion of solid state reaction. The ordering caused the lattice distortion to the orthorhombic symmetry and the doubled unit cell.

The cation vacancy ordering was also observed for La-Ti-Al-O perovskites discussed in chapter 2. It was noticed that the ordering is responsible for the dielectric relaxation and oxide ion conduction. Absence of cation vacancy ordering in the sol-gel derived $La_{2/3}TiO_3$ is probably due to a lower processing temperature.

The defect structure of the sol-gel derived PT-LT and La–Ti–O perovskite could not be determined directly from the XRD patterns because of the broad line width. Therefore, simulation of XRD patterns using the Rietveld software, RIETAN, were conducted. XRD patterns for PT-LT with $x = 0.3$, 0.6 and 1.0 shown in Fig. 3.7 were calculated from the defect model based on the weighted mean atomic scattering factor in which La^{3+} randomly replaces Pb^{2+} and makes the cation vacancies at A-site of the cubic perovskite structure with space group of $Pm3m$. The distribution of the cation vacancy is assumed to be random. The defect model was chosen from the observation of the XRD patterns in Figs. 3.3 and 3.4; (1) simple cubic perovskite patterns with $x \geq 0.3$, (2) a change in the relative peak intensities such as 100 and 200, and (3) absence of the superlattice lines. In calculation, the lattice parameters were fixed at 0.395 nm and the peak widths due to an apparatus were reproduced in order to show a variation in the relative peak intensity clearly. The broadening of peaks due to the crystallite size is not included. The variation in the relative peak intensity agrees with the experimental results shown in Figs. 3.3 and 3.4; a sharp decrease in 100 and a slight increase in 200 with increasing x are well demonstrated. Therefore, the structure of the La-Ti-O perovskite as an end member of PT-LT solid solution is considered to include cation vacancies at A-site, namely $(La_{2/3}\square_{1/3})TiO_3$.

In the previous chapter, it is concluded that the cation vacancy ordering in A-site of the perovskite structure is responsible for the enhanced oxide ion conductivity in La-Ti-Al-O ceramics. Reduced conductivity in the sol-gel derived $La_{2/3}TiO_3$ film

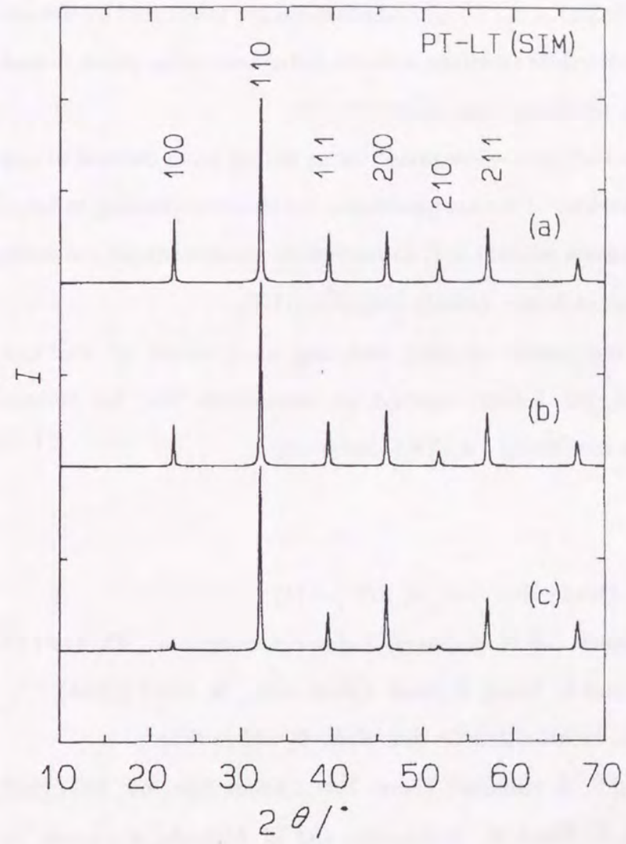

Fig. 3.7 Results of the simulation of X-ray diffraction patterns for $(1-x)PbTiO_3$-$xLa_{2/3}TiO_3$ based on the model including cation vacancies at A-site. (a) $x = 0.3$, (b) $x = 0.6$, and (c) $x = 1.0$.

shown in Fig. 3.6 is mainly due to absence of the cation vacancy ordering which was caused by the lower processing temperature in the sol-gel and dip-coating process.

3.5 Summary

(1) Thin films of $PbTiO_3$-$La_{2/3}TiO_3$ solid solutions are fabricated by the sol-gel method. They have a perovskite structure with the tetragonal-cubic phase boundary of about $x = 0.2$ and the solubility limit of $x = 0.9$.

(2) Metastable La-Ti-O perovskite phase forms with a small amount of impurity phase, $La_2Ti_2O_7$, in the film of the composition $x = 1.0$ (corresponding to $La_{2/3}TiO_3$).

(3) The defect structure of the La-Ti-O perovskite phase contains randomly distributed cation vacancies at A-site, namely $(La_{2/3}\square_{1/3})TiO_3$.

(4) Absence of the cation vacancy ordering as a result of the low processing temperature in the sol-gel method is responsible for the reduced electrical conductivity in the film of $La_{2/3}TiO_3$ composition.

References

1 D. Hennings, *Mater. Res. Bull.*, **6**, 329 (1971).

2 J. B. MacChesney and H. A. Sauer, *J. Amer. Ceram. Soc.*, **45**, 419 (1962).

3 M. Kestigian and R. Ward, *J. Amer. Chem. Soc.*, **76**, 6027 (1954).

4 M. Abe and K. Uchino, *Mater. Res. Bull.*, **9**, 147 (1974).

5 T. Y. Tien and F. A. Hummel, *Trans. Brit. Ceram. Soc.*, **66**, 233 (1967).

6 Y. Takahashi, K. Niwa, K. Kobayashi, and M. Matsuki, *J. Ceram. Soc. Jpn.*, **95**, 942 (1987).

7 F. Izumi, *Nippon Kessho Gakkaishi*, **27**, 23 (1985).

8 G. Shirane and S. Hoshino, *J. Phys. Soc. Jpn.*, **6**, 265 (1951).

9 T. Yamamoto, H. Igarashi, and K. Okazaki, *J. Amer. Ceram. Soc.*, **66**, 363(1983).

10 Y. Shimizu, K. R. Udayakumar, and L. E. Cross, *J. Amer. Ceram. Soc.*, **74**, 3023 (1991).

11 K. Kani, H. Murakami, K. Watari, A. Tsuzuki, and Y. Torii, *J. Mater. Sci. Lett.*, **11**, 1605 (1992).

12 R. D. Shannon and C. T. Prewitt, *Acta Cryst.*, **B25**, 925(1969).

13 A. V. Prasadarao, U. Selvaraj, S. Komarneni, and A. S. Bhalla, *J. Mater. Res.*, **7**, 2859 (1992).

Rapid quenching and dielectric properties of $Pb(Mg_{1/2}W_{1/2})O_3$

4.1 Introduction

Enhancement of the solubility limit by the sol-gel method was shown in chapter 1 for the system $PbTiO_3$-$MgTiO_3$. The deficient perovskite $La_{2/3}TiO_3$ with one third of A-site cation vacancy was obtained as a metastable phase in thin films also by the sol-gel method as described in chapter 3. These results clearly demonstrate that the sol-gel method is suitable for fabricating materials including a lot of defects. As for the rapid quenching method, it has been widely used for the preparation of amorphous and metastable phases. A crystallization process of the melt-quenched amorphous phases is probably similar with that occurs in heat treatment of gel states in the sol-gel method This suggests that the rapid quenching technique have a potential to create unique defect structures which have not been obtained in the equilibrium stable phases.

After Lines first proposed the possibility of ferroelectricity in an amorphous states theoretically [1], amorphous states of ferroelectric materials, such as $LiNbO_3$ [2] and $PbTiO_3$ [3] were prepared by rapid quenching and their dielectric properties were studied. Crystallization process of amorphous $LiNbO_3$ was investigated by Nasssau *et al.* [4], showing an appearance of metastable phases and anomalous dielectric properties.

Complex perovskite-type oxides are compounds with their A-sites or B-sites occupied by two different cations in a fixed proportion. Due to the various combinations and ordering of cations a wide variety of functional complex perovskite-type oxides are known.

$Pb(Mg_{1/2}W_{1/2})O_3$ (PMW) is one of those complex perovskite-type oxides in which its B-site cations, Mg^{2+} and W^{6+}, are ordered; it is antiferroelectric below the

phase transition at 314 K [5]. In this chapter, preparation of amorphous PMW by the twin-roller rapid quenching method and its dielectric properties in an amorphous state are studied. Its crystallization process and dielectric properties of annealed (recrystallized) PMW are also investigated. Drastic changes of the dielectric properties of PMW are discussed in relation to its crystal and defect structures.

4.2 Experimental

Ceramic samples used for the quenching experiments were prepared from stoichiometric proportions of PbO, MgO, and WO_3 by firing at 1073 K for 4 h, pressing into pellets, and sintering at 1173 K for 2 h. A twin-roller apparatus shown in Fig. 4.1, giving quenching rates of about 10^5-10^7 K s^{-1} [4], was used to produce rapidly quenched samples. After the pellets being melted, the melts were squirted out of the Pt crucible with a pressure of Ar and injected between rotating steel rollers. Quenched flakes were reground, and pressed into pellets. Some of these pellets were reheated at various temperatures between 673 K and 1173 K for 1 h to prepare annealed samples.

Phases were examined by X-ray powder diffraction analysis (XRD) with Cu Kα radiation. Thermal properties were investigated using a differential scanning calorimeter (DSC) with a scanning rate of 20 K min^{-1}.

For dielectric measurements, pellets were polished and Pt-Pd electrodes were sputtered onto both surfaces. Dielectric constant and loss as a function of temperature (173 K to 873 K) and frequency (1 kHz to 10 kHz) were measured with the three-probe method in a field of 50 V cm^{-1} using a YHP 4274A LCR meter.

4.3 Results

Formation of an amorphous state

Roller-quenched flakes were yellowish and glossy. An XRD pattern of ground flakes quenched under an optimum condition evidently shows the formation of an amorphous state (Fig. 4.2(b)). A few diffraction lines of crystalline Pb_2WO_5 are

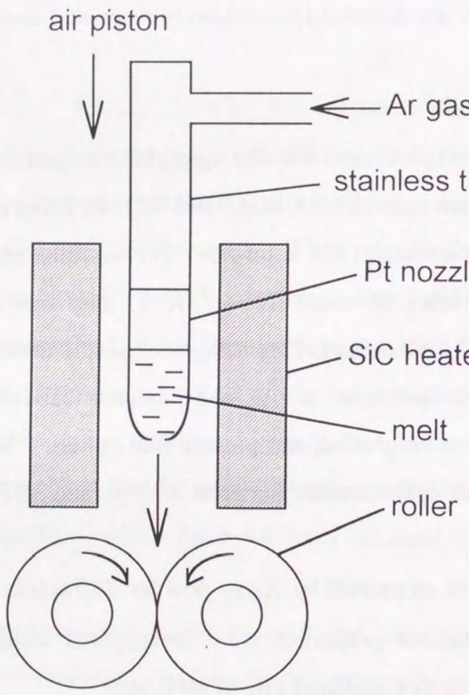

Fig. 4.1 A twin-roller apparatus used for quenching $Pb(Mg_{1/2}W_{1/2})O_3$.

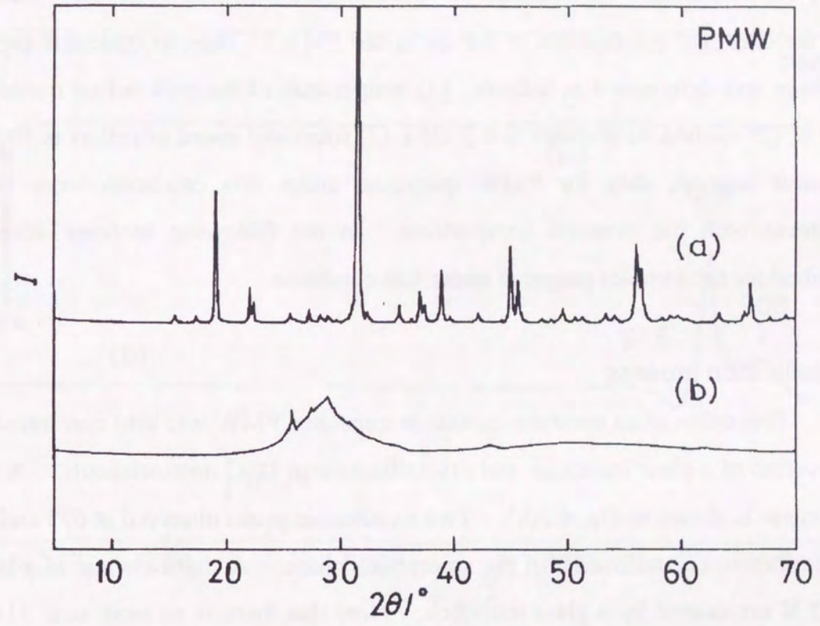

Fig. 4.2 X-ray diffraction patterns of (a) sintered and (b) quenched $Pb(Mg_{1/2}W_{1/2})O_3$.

observed, indicating that it contained somewhat crystalline regions even in the optimum condition.

A decrease in applied Ar pressure and rotational speed of rollers resulted in an increase in Pb_2WO_5 content because of a decrease in a quenching rate. The amount of Pb_2WO_5 decreased with elevating temperature of the melt before quenching. But above 1400 K, intense volatilization of PbO from the melt was observed. This might shift the chemical composition of the quenched PMW. Thus an optimum quenching condition was determined as follows : (1) temperature of the melt before quenching is 1400 K, (2) applied Ar pressure is 0.2 MPa, (3) rotational speed of rollers is 5000 rpm. Chemical analysis data for PMW quenched under this condition were in good agreement with the nominal composition. In the following sections, results are described for the samples prepared under this condition.

Crystallization process

Formation of an amorphous state in quenched PMW was also confirmed by an observation of a glass transition and crystallization in DSC measurements. A typical DSC curve is shown in Fig. 4.3(b). Two exothermic peaks observed at 675 and 700 K are ascribed to crystallization of the amorphous phase. A slight change of a baseline at 645 K are caused by a glass transition. Note that there is no peak near 314 K, at which temperature an orthorhombic-cubic phase transition occurs and a sharp endothermic peak is observed for sintered PMW (Fig. 4.3(a)).

Crystalline phases which appeared on heating above the crystallization temperature were next examined. In a sample annealed at 873 K for 1 h, three phases were identified from XRD analysis : (A) perovskite type $Pb(Mg_{1/2}W_{1/2})O_3$, (B) scheelite type $PbWO_4$, and (C) orthorhombic Pb_2WO_5 (Fig. 4.4). Contents of the above three phase in the samples annealed at various temperatures were estimated from the intensity of the strongest XRD peak of each phase (Fig. 4.5). $PbWO_4$ and Pb_2WO_5, passing through the maximum at 873 K, decreased to a small value with the elevation of annealing temperature. In contrast, $Pb(Mg_{1/2}W_{1/2})O_3$ monotonously

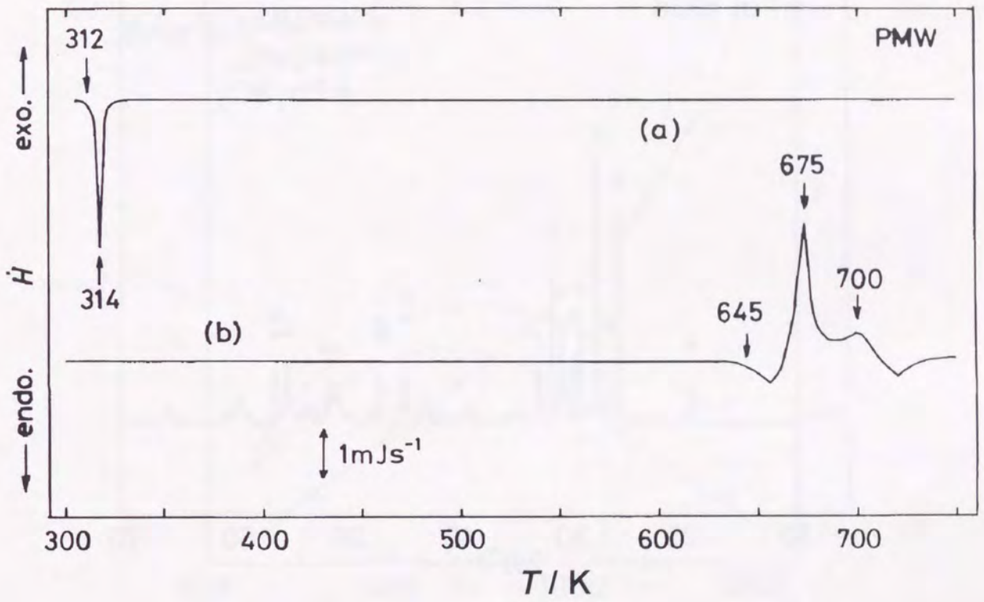

Fig. 4.3 Typical DSC curves of (a) sintered and (b) quenched $Pb(Mg_{1/2}W_{1/2})O_3$.

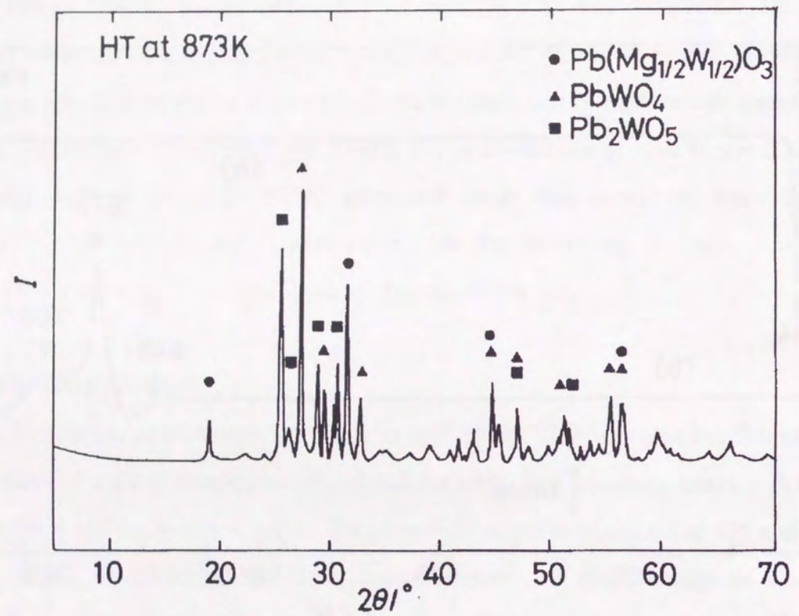

Fig. 4.4 X-ray diffraction pattern of $Pb(Mg_{1/2}W_{1/2})O_3$ annealed at 873 K for 1 h.

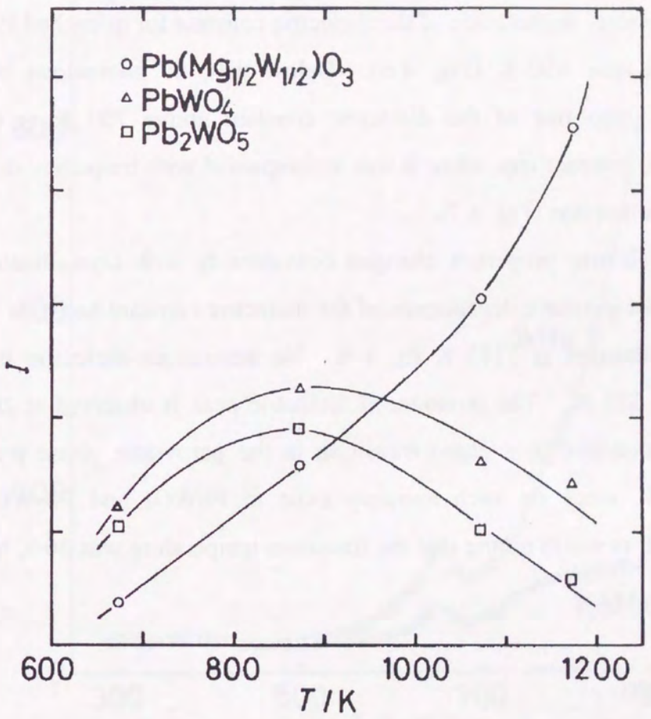

Fig. 4.5 Effects of annealing temperature on the crystalline phases appeared.

increased with increasing annealing temperature. Even at the highest annealing temperature of 1173 K, however, the single perovskite phase was not obtained for annealed PMW.

Dielectric properties

Temperature dependence of the dielectric constant for quenched PMW showed a diffuse peak near 650 K (Fig. 4.6). Below that, no anomalous behavior was observed. A steep rise of the dielectric constant above 700 K is attributed to increasing ionic conductivity, since it was accompanied with frequency dispersion and a dielectric loss increase (Fig. 4.7).

The dielectric properties changed considerably with crystallization. Figure 4.8 shows the temperature dependence of the dielectric constant between 173 and 373 K for PMW annealed at 1173 K for 1 h. No anomalous dielectric behavior was detected above 373 K. The pronounced dielectric peak is observed at 283 K. This peak can be attributed to a phase transition in the perovskite phase precipitated in annealed PMW, since no such anomaly exist in $PbWO_4$ and Pb_2WO_5 near this temperature. It is worth noting that the transition temperature was 30 K below that of sintered PMW.

4.4 Discussion

Dielectric properties of quenched PMW

Dielectric properties of amorphous states of ferroelectric materials such as $LiNbO_3$ and $PbTiO_3$ have been studied. Glass *et al.* [2] reported that amorphous $LiNbO_3$ showed a dielectric anomaly 150 K below the crystallization temperature. They suggested that it was a ferroelectric transition. But amorphous $PbTiO_3$ and $LiNbO_3$-BaO measured by Takashige *et al.* [3] and Tatsumisago *et al.* [6], respectively, showed no evidence of ferroelectric transitions.

The dielectric constant of quenched PMW showed a peak near 650 K (Fig. 4.6). This temperature is between its glass transition and crystallization temperature

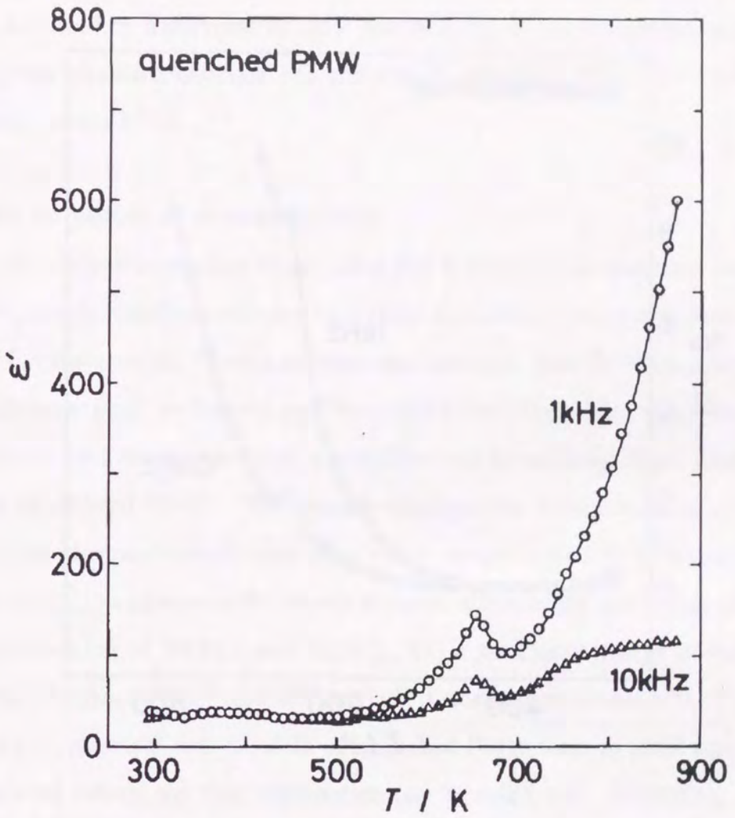

Fig. 4.6 Temperature dependence of the dielectric constant for quenched $Pb(Mg_{1/2}W_{1/2})O_3$.

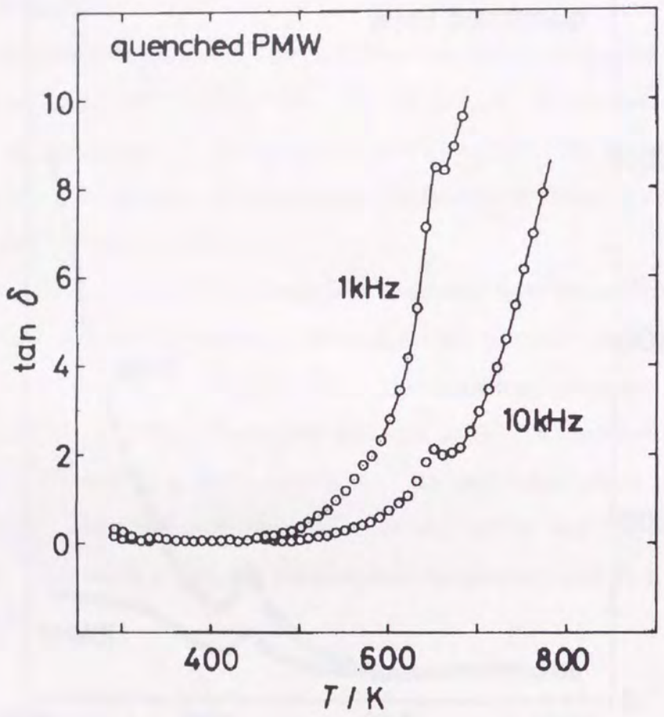

Fig. 4.7 Temperature dependence of the dielectric loss for quenched $Pb(Mg_{1/2}W_{1/2})O_3$.

measured by DSC (Fig. 4.3). Furthermore the dielectric loss showed a peak at the same temperature (Fig. 4.7). Hence the dielectric behavior near 650 K can be explained by an increase of ionic conductivity due to relaxation of a frozen ionic motion, followed by a decrease of ionic conductivity due to crystallization. Since no anomaly was observed between 173 and 650 K, quenched PMW is considered to be paraelectric above 173 K.

Dielectric properties of annealed PMW

The dielectric constant of annealed PMW showed a pronounced peak at 283 K (Fig. 4.8), which could be attributed to a phase transition of the precipitated perovskite phase. Evidence of the phase transition was obtained from DSC measurements with an endothermic peak on heating and its reversibility (Fig. 4.9). This transition was characterized by a lower transition temperature and broadening of the peak compared with that of sintered PMW. The possible explanations for them are as follows: (1) a change in the chemical composition of an entire sample caused by volatilization of PbO from the melt, (2) a change in the chemical composition of the perovskite phase caused by co-precipitation of $PbWO_4$ and Pb_2WO_5, (3) a structural change in the perovskite phase (the ordering of Mg^{2+} and W^{6+}) and (4) distortions in the perovskite structure.

Since chemical analysis data of quenched PMW were in good agreement with the calculated values, the first explanation can be ruled out. Regarding to the third one, if the degree of ordering changes, relative intensity of the superlattice line would change as is observed in $Ba(Mg_{1/3}Nb_{2/3})O_3$ (BMN) and $Ba(Zn_{1/3}Nb_{2/3})O_3$ (BZN). It was found, from the preliminary experiment, that the intensities of superlattice lines in BMN increased with increasing sintering temperature, indicating a steady increase in the degree of ordering. As for BZN the superstructure lines were observed up to the sintering temperature of 1673K, but no superstructure lines were detected at 1773K. This clearly shows that the degree of ordering in BZN drastically changed between 1673K and 1773K and the order-disorder transition exists.

In the case of annealed PMW, XRD data evidently shows the superlattice line

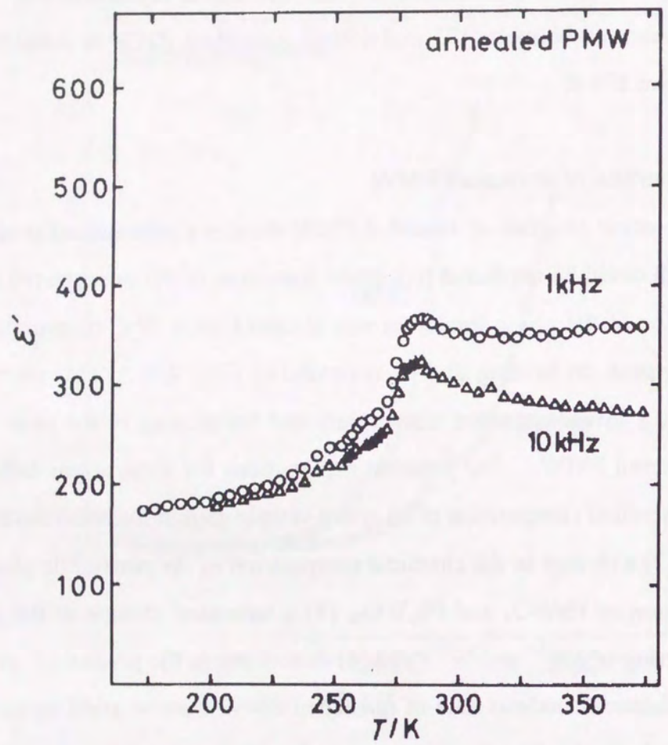

Fig. 4.8 Temperature dependence of the dielectric constant for annealed $Pb(Mg_{1/2}W_{1/2})O_3$.

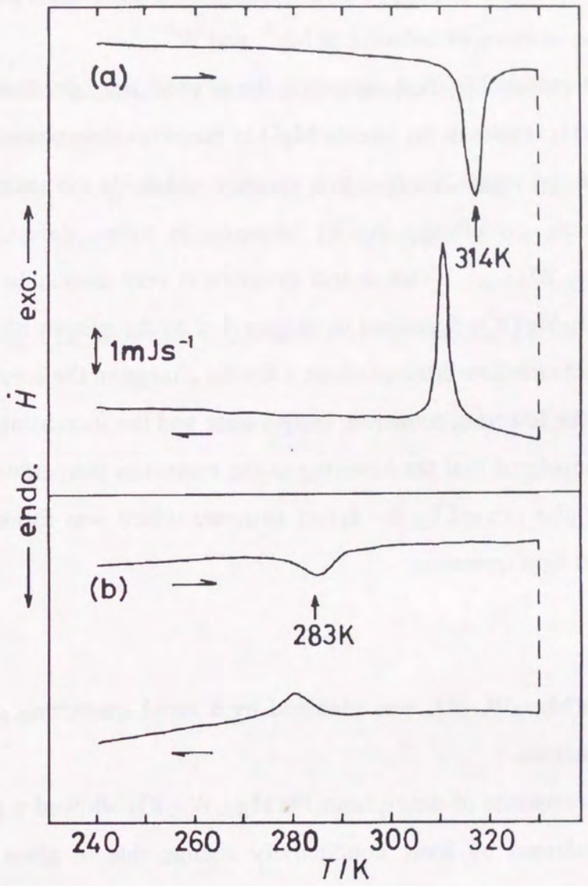

Fig. 4.9 DSC curves of the phase transition in (a) sintered and (b) annealed $Pb(Mg_{1/2}W_{1/2})O_3$.

at $2\theta \sim 19°$, indicating the ordering of Mg^{2+} and W^{6+} (Fig. 4.4). The intensity ratio of the superlattice line to the strongest diffraction line for annealed PMW was almost equal to that for sintered PMW. Thus the precipitated perovskite phase is identical with a sintered one in terms of ordering of Mg^{2+} and W^{6+}.

The most reasonable explanation is the second one; precipitation of stable $PbWO_4$ and Pb_2WO_5 results in the excess MgO in the perovskite phase. Excess MgO would enter B-site and create A-site cation vacancy and oxide ion vacancy to maintain a charge balance, resulting in a change in the defect structure as $Pb_{1-y}(Mg_{(1+x)/2}W_{(1-x)/2})O_{3-2x-y}$. This defect structure is very similar to that of the sol-gel derived $PbTiO_3$-$MgTiO_3$ described in chapter 1. In the system $PbTiO_3$-$MgTiO_3$ a change in the defect structure brought about a drastic change in the electrical properties as is observed by the lowering transition temperature and the increasing dielectric loss. Therefore, it is considered that the lowering in the transition temperature observed for annealed PMW is also caused by the defect structure which was formed during rapid quenching and post heat treatment.

4.5 Summary

(1) Amorphous $Pb(Mg_{1/2}W_{1/2})O_3$ was obtained by a rapid quenching method using a twin-roller apparatus.

(2) The dielectric constants of amorphous $Pb(Mg_{1/2}W_{1/2})O_3$ showed a peak at 650 K, which was explained by ionic conductivity change due to glass transition and crystallization of amorphous $Pb(Mg_{1/2}W_{1/2})O_3$.

(3) Annealing of amorphous $Pb(Mg_{1/2}W_{1/2})O_3$ does not form the single phase perovskite on crystallization, but results in three crystalline phases, $Pb(Mg_{1/2}W_{1/2})O_3$, $PbWO_4$ and Pb_2WO_5.

(4) A change in the defect structure created by excess MgO in the perovskite phase causes lowering of the phase transition temperature about 30 K in annealed $Pb(Mg_{1/2}W_{1/2})O_3$.

References

1 M. E. Lines, *Phys.Rev.B*, **15**, 388 (1977).

2 A. M. Glass, M. E. Lines, K. Nassau and J. W. Shiever, *Appl. Phys. Lett.*, **31**, 249 (1977).

3 M. Takashige, T. Nakamura, H. Ozawa, R. Uno, N. Tsuya and K. Arai, *Jpn. J. Appl. Phys.*, **19**, L249 (1980).

4 K. Nassau, C. A. Wang, and M. Grasso, *J. Am. Ceram. Soc.*, **62**, 74 (1979).

5 S. Nomura, S. J. Jang, L. E. Cross and R. E. Newnham, *J. Am. Ceram. Soc.*, **62**, 458 (1979).

6 M. Tatsumisago, A. Hamada, T. Minami and M. Tanaka, *J. Am. Ceram. Soc.*, **65**, 575(1982).

High pressure synthesis of Bi-Sr-Ca-Cu-O superconductors

5.1 Introduction

Phase stability changes with pressure. Phases prepared under high pressure often keep their crystal structures after releasing pressure. Thus, phases which are not prepared at atmospheric pressure can be obtained as metastable phases.

Bi-Sr-Ca-Cu-O superconductors have three kinds of crystalline phases which are called as 2201, 2212 and 2223 phases as shown in Fig. 5.1. Their *c* cell dimensions are 2.5, 3.0 and 3.6 nm, and their superconducting transition temperatures are 20, 80 and 110 K, respectively [1]. To prepare the dense Bi-Sr-Ca-Cu-O superconductors hot press and hot isostatic press were studied [2]-[4]. In these study the starting materials for high pressure treatments are superconducting powders prepared at atmospheric pressure.

The author used mixed powder of oxides as starting materials to study direct synthesis of Bi-Sr-Ca-Cu-O superconducting phases. Phase stabilities, microstructures, and superconducting properties of Bi-Sr-Ca-Cu-O phases prepared under high pressure was also evaluated.

5.2 Experimental

Three kinds of starting powders, (A), (B) and (C), were used for high pressure synthesis. Sample (A) was a powder of Bi_2O_3, SrO, CaO, and CuO mixed with the composition Bi:Sr:Ca:Cu=2:2:2:3. To prepare sample (B), (A) was calcined at 1123 K for 24 h and ground. The 2212 phase and CuO were found in the sample (B) by X-ray diffraction (XRD) analysis. Sample (C) was a ground powder of a sintered $Bi_{1.6}Pb_{0.4}Sr_2Ca_2Cu_3O_z$ pellet. The 2223 single phase (high T_c-phase) was found by XRD analysis.

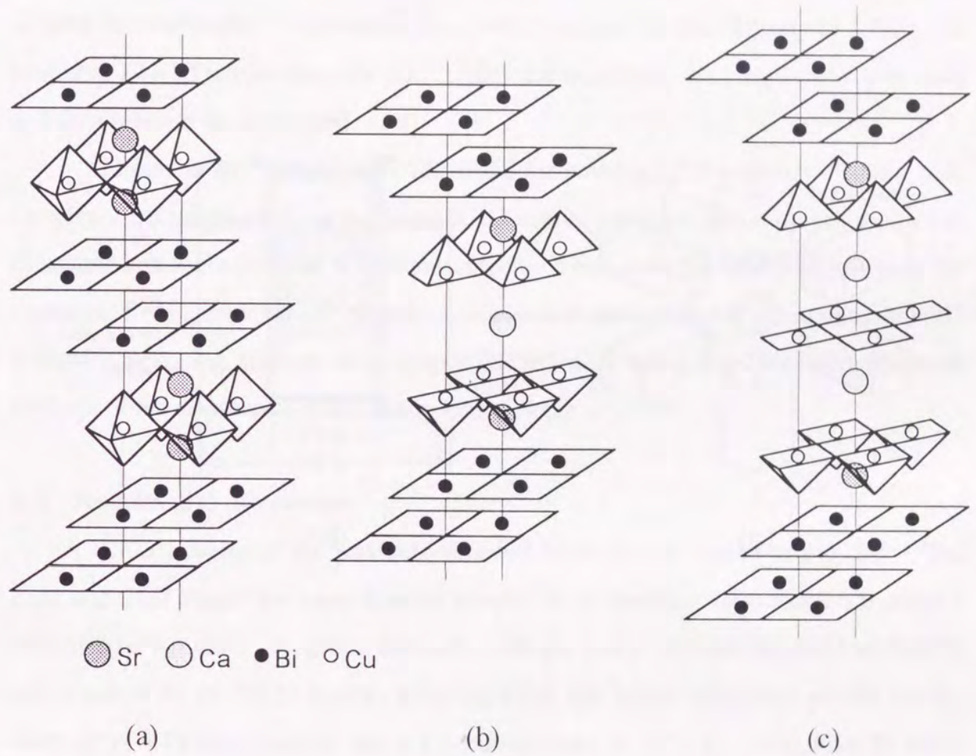

Fig. 5.1 Crystal structures of $Bi_2Sr_2Ca_{n-1}Cu_nO_{3n+4}$. (a) $n = 1$, $T_c = 6$ - 20 K, (b) $n = 2$, $T_c = 80$ K and (c) $n = 3$, $T_c = 105$ K.

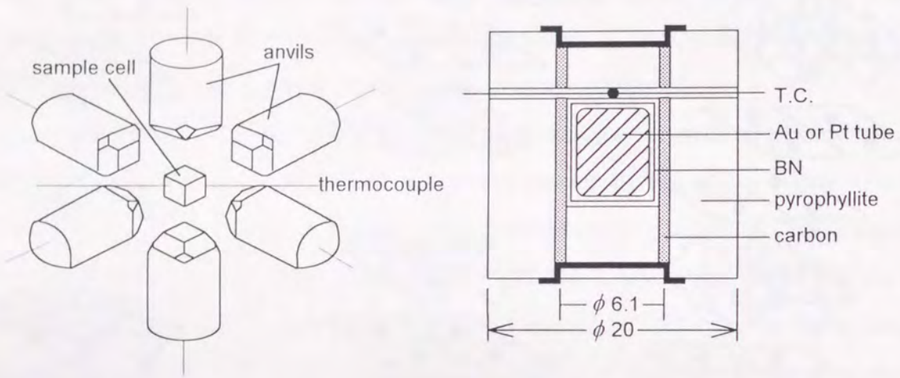

Fig. 5.2 Apparatus for high pressure synthesis. (a) Cubic anvil-type generator and (b) cell.

High pressure synthesis was carried out using a cubic anvil-type apparatus shown in Fig. 5.2. Starting powder was encapsulated into a gold or platinum tube of 6 mm in diameter and inserted in a BN container. This assemblage was placed in the center of a pyrophyllite cube (20×20×20 mm) along with a carbon heater and a Pt-13%Rh thermocouple. The sample was pressed almost isostatically up to 3 GPa and heated at a fixed temperature for 6 h. After the treatment, the sample was quenched and then pressure was released.

Phases in the sample were identified by powder XRD analysis. Some bulk samples were subjected to micro-focus XRD analysis without grounding to a powder. Electrical resistivity at 4-300 K was measured by a two-terminal method because of the limitation from sample size. Magnetic data were measured at 4 K using an rf-SQUID method. Scanning electron micrographs (SEM) were taken for Au-coated fractured surfaces of the samples with an acceleration voltage of 20 kV.

5.3 Results and discussion

XRD patterns of the products obtained from (A) are shown in Fig. 5.3. The 2201 and CuO phases are formed in the sample (A-1) heated at 1003 K for 6 h under 3 GPa using a Au tube. Reaction between a sample and a Au tube occurred at 1043 K and resulted in an XRD pattern different from the superconducting phases (A-2). With using a Pt tube reaction did not occurred even at 1073 K. Therefore Pt tubes were used for further experiments.

Also for the sample reacted at 1073 K (A-3), an XRD pattern similar to the 2201 was obtained. A change in the intensity ratio though, *e.g.* large 115 peak intensity, was observed. In addition, a split in the 002 peak was observed and *c* cell dimensions obtained for each phases are 2.48 and 2.39 nm. The phase of $c = 2.48$ nm is 2201 ($Bi_2Sr_2CuO_z$). Fujiwara [5] reported that 50 % of Sr^{2+} can be replaced by Ca^{2+} in the 2201 phase prepared by a self flux method, resulting in a decrease in the c cell dimension to 2.43 nm. The phase of $c = 2.39$ nm in A-3 probably has a structure in which BiO_2, CuO, and Ca-rich Sr-Ca-O planes were compressed and stabilized under

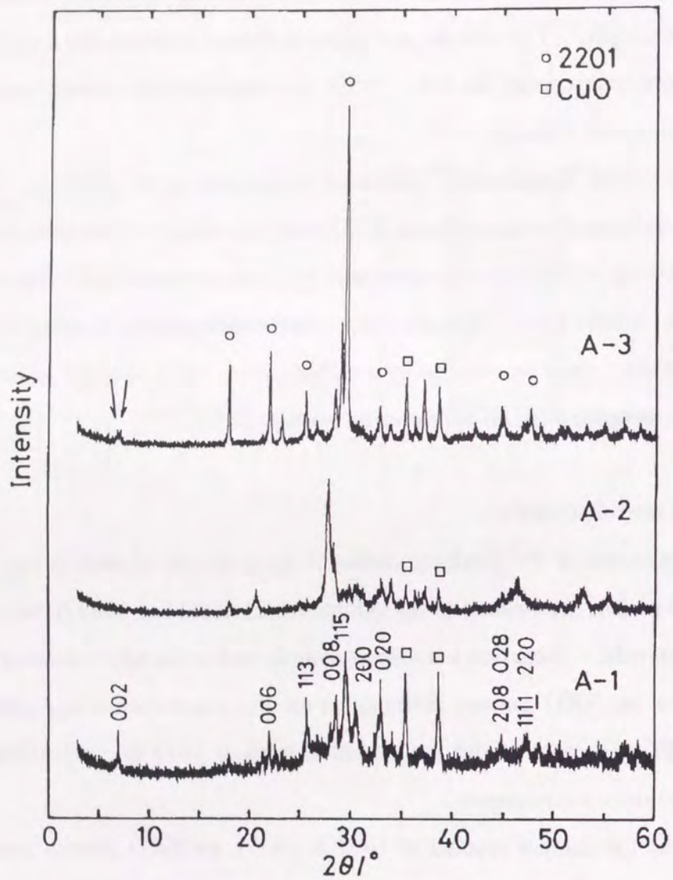

Fig. 5.3 X-ray diffraction patterns of Bi-Sr-Ca-Cu-O prepared from mixed oxides under 3 Gpa at various conditions. A-1 : 1003 K using Au capsule, A-2 : 1043 K using Au capsule, A-3 : 1073 K using Pt capsule.

high pressure.

Figure 5.4 shows XRD patterns of the products starting from (B). The 2212 and CuO phases existed in the starting material (B-0). An XRD pattern similar to the 2201 phase was obtained after the treatment at 1073 K for 6 h under 3 GPa (B-1). The sample treated at 1103 K (B-2) also shows the 2201-type XRD pattern, and a split in the 002 diffraction peak is seen as in the case of A-3.

Furthermore, even starting from the 2223 phase, the 2201-type phase is formed after the treatment at 1103 K under 3 GPa as shown in Fig. 5.5 (C-1). The split in the 002 diffraction peak though is not seen. Above XRD results show that both the 2212 and 2223 phases change to the 2201-type phase after the high pressure treatment.

Starting materials, experimental conditions, and phases identified by powder XRD analysis after the treatment are summarized in Table 5.1. It is concluded that the 2201-type phase is formed under pressure of 3 GPa with starting from the oxide mixture, 2212 and 2223 phases. It is considered that the 2201 phase which has the shortest c cell dimension is the most stable among these phases under high isostatic pressure. The phase stability under high pressure can be evaluated from the density. Lattice parameters for the 2201 phase are a = 0.3801 nm, c= 2.462 nm, and Z = 2 [6], and the density is 7.03 g cm^{-1}. Using a = 0.3814 nm and c = 3.052 nm for the 2212

Table 5.1 Conditions of high pressure synthesis and phase identified in the products by powder X-ray diffraction measurements

sample	starting powder	capsule	p / GPa	T / K	t / h	phases
A-1	mixed oxides	Au	3	1003	6	2201, CuO
A-2	mixed oxides	Au	3	1043	6	unknown
A-3	mixed oxides	Pt	3	1073	6	2201(*), CuO
B-1	2212-phase	Pt	3	1073	6	2201, CuO
B-2	2212-phase	Pt	3	1103	6	2201(*)
C-1	2223-phase	Pt	3	1103	6	2201, CuO

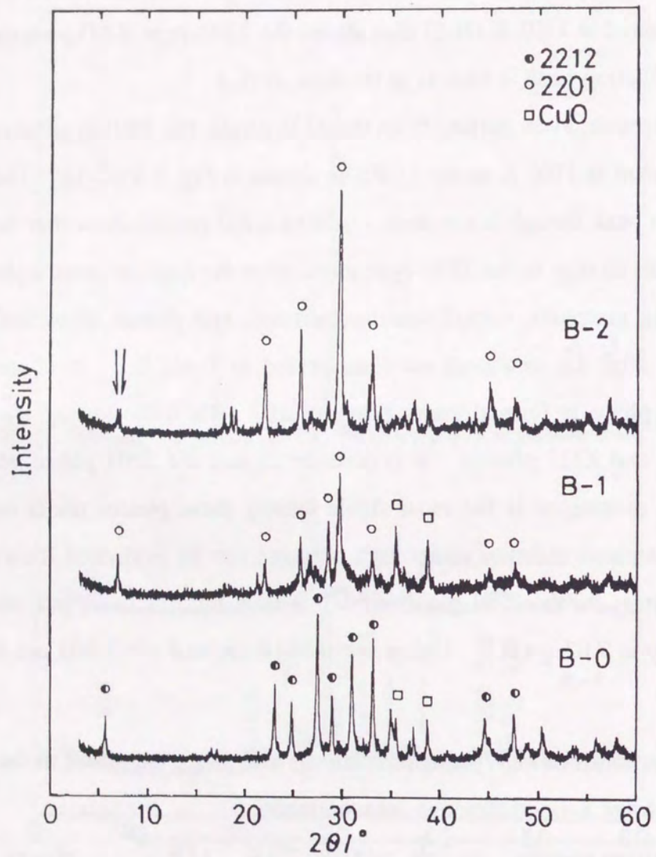

Fig. 5.4 X-ray diffraction patterns of Bi-Sr-Ca-Cu-O prepared from 2212-phase under 3 Gpa at various conditions. B-0 : starting powder, B-1 : 1073 K using Pt capsule, B–2 : 1103 K using Pt capsule.

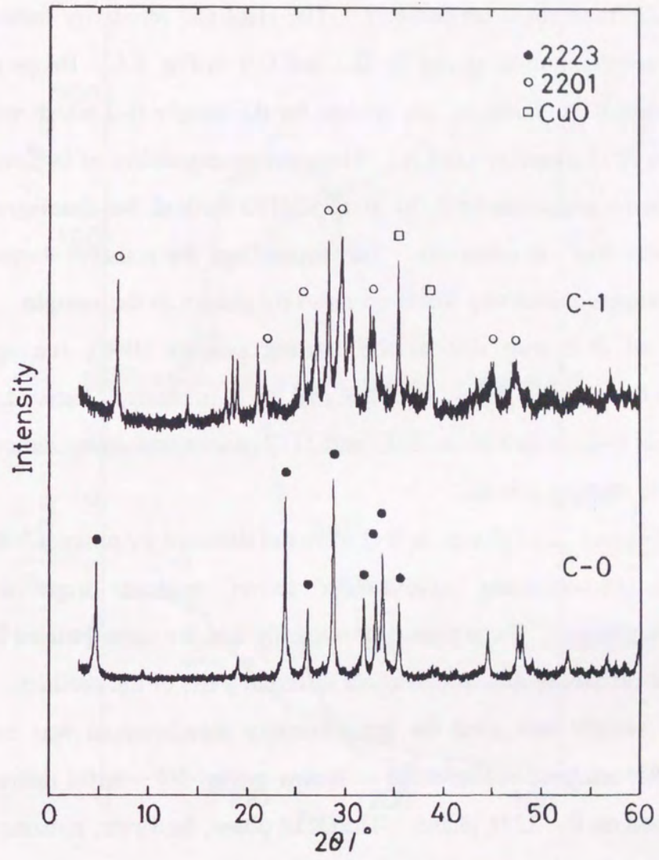

Fig. 5.5 X-ray diffraction patterns of Bi-Sr-Ca-Cu-O prepared from 2223-phase under 3 Gpa at various conditions. C-0 : starting powder, C-1 : 1073 K using Pt capsule.

phase and a = 0.38 nm and c = 3.6 nm for the 2223 phase, calculated densities of the 2212 and 2223 phases are 6.66 and 6.56 gcm^{-1}, respectively. The 2201 phase have the highest density and is supposed to be the most stable under high pressure.

The samples obtained under high pressure showed high electrical resistivity of more than 1 kΩ cm at room temperature. The electrical resistivity further increased with lowering temperature as shown by B-1 and C-1 in Fig. 5.6. Drops in resistivity around 110 K and 80 K, however, are evident for the sample B-2 which were prepared by pressing the 2212 phase at 1103 K. Magnetic susceptibility of B-2 was measured at 4 K to confirm superconductivity by an rf-SQUID method, but diamagnetism due to superconductivity was not observed. This means that the resistive drops are caused not from bulk superconductivity but from minority phases in the sample. Comparing the resistivity of B-2 with that of the starting powder (B-0), the agreement in temperature of the resistive drops at 110 K and 80 K is clearly observed. Thus, the resistive drops in B-2 are due to the 2223 and 2212 phases remaining somewhere in the product from the starting powder.

The 2223 and 2212 phases in B-2 were not detected by powder XRD analysis. The resistivity measurement nevertheless shows evident drops due to the superconductive phases. The reason is presumably that the samples used for the XRD analysis and the resistivity measurement are different parts of the product. Therefore, the same bulk sample that used for the resistivity measurement was examined by micro-focus XRD analysis. The result is shown in Fig. 5.7. Most diffraction peaks are indexed based on the 2201 phase. The 2212 phase, however, remains in this part as marked by triangles.

Scanning electron micrographs for fractured surfaces of the samples are shown in Fig. 5.8. A-1 prepared under high pressure from the oxide mixture has larger grain size and a more dense packing than B-0 prepared at atmospheric pressure. Moreover, A-3 prepared at 1073 K gives traces of liquid phase sintering. B-1 and B-2 prepared from the 2212 phase also shows grain growth and densification. Highly oriented structure of the grains is seen here and there for B-2. It is considered that the highly

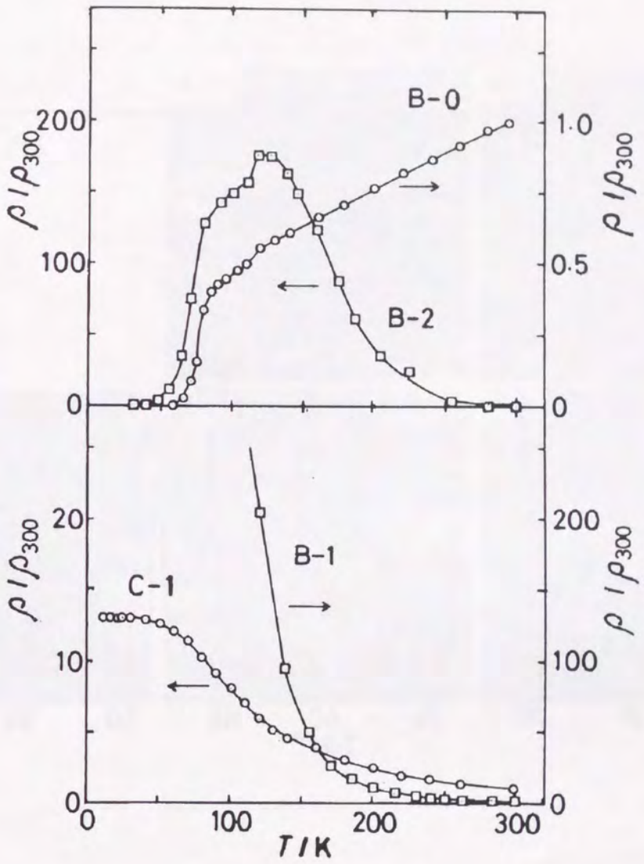

Fig. 5.6 Temperature dependences of electrical resistivity of B-0, B-1, B-2, and C-1 samples.

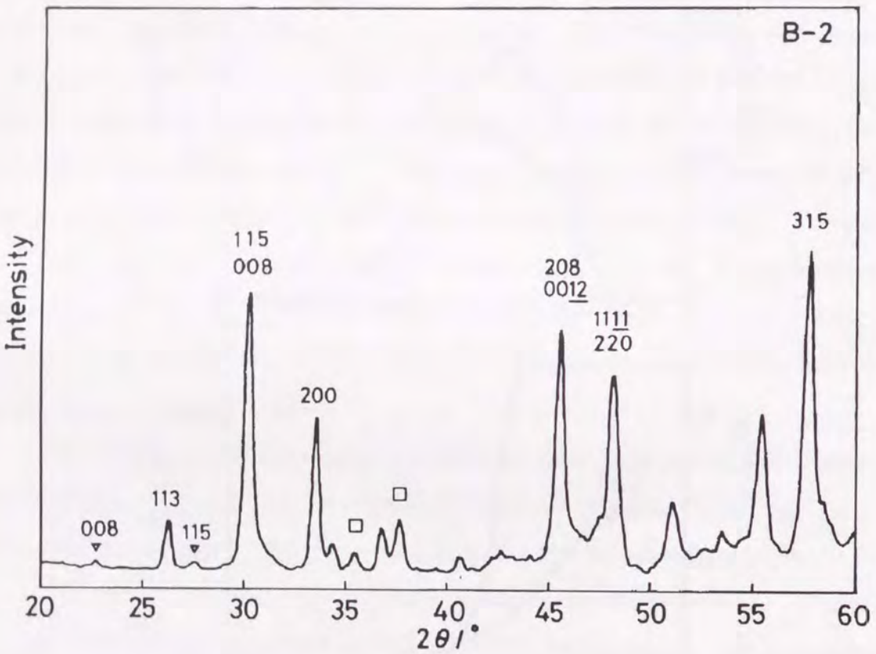

Fig. 5.7 X-ray micro-diffraction pattern of B-2 sintered body.

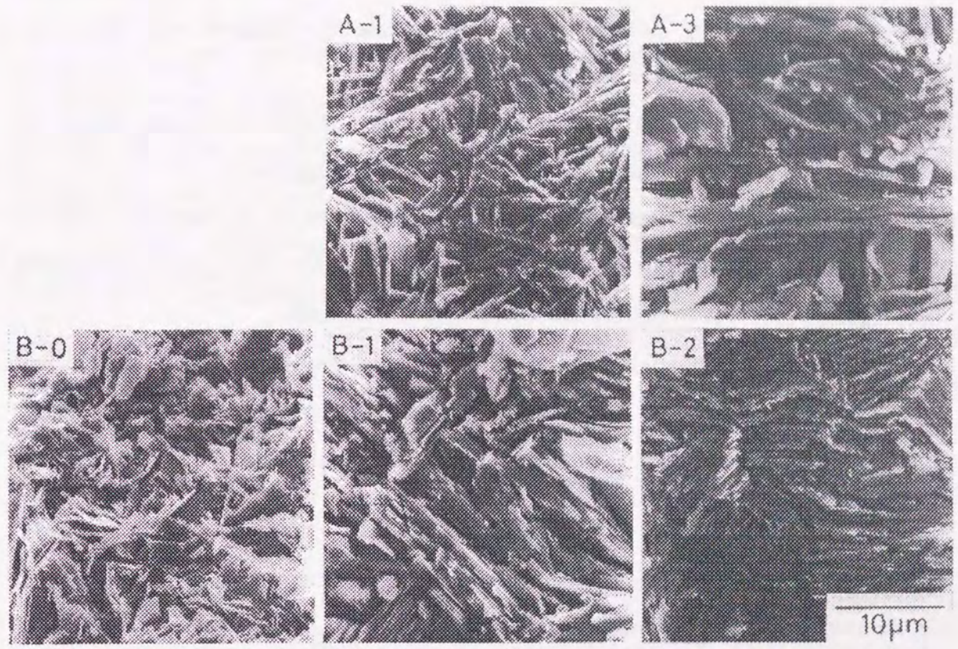

Fig. 5.8 Scanning electron micrographs of fractured surfaces for A-1, A-3, B-0, B-1, and B-2 samples.

oriented structure of the remaining superconducting phases is responsible for the resistive drops observed for B-2.

5.4 Summary

(1) The 2201 phase was formed in the product prepared under 3 GPa from the oxide mixture in 2212 ratio. Both 2212 and 2223 phases also changed to the 2201-type phase after the high pressure treatment.

(2) The formation of the 2201-type phase under high pressure is probably due to its highest density among the Bi-Sr-Ca-Cu-O superconducting phases.

(3) A split of the 002 diffraction line is observed in some of the samples. This is probably due to the mixture of 2201 phases. The smaller *c*-axis phase has Ca-rich SrO layers which was formed in the high pressure treatment.

(3) The hot pressed samples have relatively high resistivity more than 1 kΩ cm and semiconducting behavior. The samples prepared at 1103 K from the 2212 phase showed resistive drops due to remaining superconducting phases.

References

1 K. Kitazawa and K. Kishio, *Oyo Buturi*, **57**, 1644 (1988).

2 H. Seino, K. Ishizaki, and M. Takata, *Jpn. J. Appl. Phys.*, **28**, L78 (1989).

3 H. Ikeda, R. Yoshizaki, K. Yoshikawa, and N. Tomita, *Jpn. J. Appl. Phys.*, **29**, L430 (1990).

4 H. Enami, N. Kawahara, T. Shinohara, S. Kawabata, H. Hoshizaki, A. Matsumoto, and T. Imura, *Jpn. J. Appl. Phys.*, **28**, L377 (1989).

5 Fujiwara, private communication.

6 H. Sawa, H. Fujiki, K. Tmimoto and J. Akimitsu, *Jpn. J. Appl. Phys.*, **27**, L830 (1988).

Conclusions

In this study, the relation between defect structures and electrical properties in the perovskite-type oxides is investigated. Effects of processing methods such as sol-gel method, rapid quenching method and high pressure synthesis on the defect structures are also examined.

General Introduction presented purpose, methods and materials in this study. In Chapter 1, solid solutions in $PbTiO_3$-$MgTiO_3$ were prepared by the sol-gel method. Enhancement of the solubility limit of Mg^{2+} in the perovskite structure was revealed. The defect structure was investigated from a change in the electrical properties with forming solid solutions. In Chapter 2, it was found that A-site deficient perovskite structure can be stabilized by a small amount of Al addition. Remarkable dielectric relaxation and high ionic conductivity were observed in the La-Ti-Al-O ceramics. It is considered that cation vacancy ordering is responsible for the oxide ion conduction. In Chapter 3, perovskite phases in $PbTiO_3$-$La_{2/3}TiO_3$ thin films including a metastable $La_{2/3}TiO_3$ phase were prepared by the sol-gel method. The defect structure and electrical properties were compared to the La-Ti-Al-O ceramics. In Chapter 4, changes in the dielectric properties of $Pb(Mg_{1/2}W_{1/2})O_3$ was discussed in relation to both crystal and defect structures changed during the rapid quenching and post heat treatment. In Chapter 5, high pressure synthesis of Bi-based superconductors is described. It was found that the defect structure including CaO-rich SrO layers was formed during the high pressure treatment.

From these results, the relations between processing methods and defect structure, and electrical properties are summarized as follows.

Processing method and defect structures

Characteristic defect structures were obtained by the sol-gel method. Enhancement of Mg^{2+} solubility was observed in sol-gel derived $PbTiO_3$-$MgTiO_3$. Mg^{2+} incorporation in B-site of the perovskite structure created vacancy in both A-site cation and oxide ion sites. In sol-gel derived $PbTiO_3$-$La_{2/3}TiO_3$ films cation vacancy were randomly distributed in A-site in contrast to the cation vacancy ordering in La-Ti-Al-O ceramics. Moreover, in the end composition of the solid solutions, $La_{2/3}TiO_3$, the perovskite phase which is not listed in a La_2O_3-TiO_2 phase diagram was formed as a metastable phase. The sol-gel method has characteristics of well-mixed starting materials and low processing temperature which can stabilize the defect structure including vacancy and result in the solubility enhancement and formation of metastable phase.

Rapid quenching from the melt realized an amorphous phase of $Pb(Mg_{1/2}W_{1/2})O_3$. The amorphous phase crystallized to a perovskite structure by the post heat treatment. However, coprecipitation of $PbWO_4$ and Pb_2WO_5 changed the composition to MgO-rich perovskite phase and caused the defect structure of $Pb_{1-y}(Mg_{(1+x)/2}W_{(1-x)/2})O_{3-2x-y}$. A combination of rapid quenching and post heat treatment has possibility of making a characteristic defect structure.

As for the high pressure synthesis of Bi-based superconductors, the most dense 2201 phase was formed in which Ca-rich SrO layers are included. This means that the high pressure synthesis has the possibility for solubility enhancement due to a change in ionic radius with pressure.

It was shown by this study that these new processing methods offer an opportunity for making unique defect structures. Especially the sol-gel method has a great potential because it requires no special apparatus and has an advantage in film preparation.

Defect structures and electrical properties

Electrical properties changed greatly if the formation of solid solutions brings about a change in the defect structure. A sharp decrease in the ferroelectric transition temperature was observed in sol-gel derived $PbTiO_3$-$MgTiO_3$ by the enhancement of the solubility limit. In addition, *p*-type conduction was observed in air as a result of the defect structure. A similar lowering of the phase transition temperature was found in $Pb(Mg_{1/2}W_{1/2})O_3$ subjected to rapid quenching and post heat treatment, in which the defect structure was formed by the excess MgO composition, resulting in the change in the electrical properties.

La-Ti-Al-O ceramics have A-site cation vacancies in an ordered way and show high oxide ion conductivity. Contrarily, random distribution of cation vacancies was found in a sol-gel derived $La_{2/3}TiO_3$ film which shows very low conductivity. Thus it was concluded that the ordering of A-site cation vacancy is responsible for oxide ion conduction in La-Ti-Al-O ceramics. This means that an arrangement of vacancy can produce new electrical properties in the perovskite-type oxides.

List of publications

Chapter 1

1 H.Yoshioka, "Dieletric properties of $PbTiO_3$-$MgTiO_3$ metastable solid solutions prepared by the sol-gel method", *J. Ceram. Soc. Jpn.*, **98**, 922 (1990)

2 H. Yoshioka, "Electrical properties and defect structure of $PbTiO_3$-$MgTiO_3$ solid solution prepared by the sol-gel method", (in preparation).

Chapter 2

3 H.Yoshioka, "Unusual dielectric behavior of La-Ti-Al-O ceramics with perovskite structure", *Jpn. J. Appl. Phys.*, **33**(7A), L945 (1994)

4 H. Yoshioka and S. Kikkawa, "Oxide ion conduction in A-site deficient La-Ti-Al-O perovskite", *J. Mater. Chem.*, **8**(8), 1821 (1998)

Chapter 3

5 H.Yoshioka, "X-ray diffraction analysis for thin films of $PbTiO_3$-$La_{2/3}TiO_3$ prepared by the sol-gel method", *J. Mater. Res.*, **9**, 2133 (1994)

Chapter 4

6 H.Yoshioka, "Ordering of cations in $Ba(Mg_{1/3}Nb_{2/3})O_3$ amd $Ba(Zn_{1/3}Nb_{2/3})O_3$", *Bull.Chem.Soc.Jpn.*, **60**, 3433 (1987)

7 H.Yoshioka, "Rapid quenching and dielectric properties of $Pb(Mg_{1/2}W_{1/2})O_3$", *J.Ceram.Soc.Jpn.*, **97**, 355 (1989)

Chapter 5

8 H.Yoshioka, S.Kikkawa, F.Kanamaru, and Y.Miyamoto, "High pressure fabrication of Bi-Sr-Ca-Cu-O superconducting ceramics", *J. Jpn. Soc. Powder and Powder Metallugy*, **37**, 755 (1990)

List of supplementary publications

1 H.Yoshioka, "Lattice parameters of sol-gel derived metastable ZrO_2-CaO solid solution", *Bull. Chem. Soc. Jpn.*, **65**, 2756 (1992)

2 H.Yoshioka, T.Ishihara, and M.Motoyama, "Characterization of ZrO_2 thin films prepared from zirconium alkoxide by sol-gel or CVD methods", Advanced Materials '93, I/A, ed. by N.Mizutani et.al., Elsevier science B.V.(1994) p.735

Acknowledgment

The author would like to express his sincere appreciation to Professor Gin-ya Adachi of Osaka University for his guidance and encouragement in coordinating this investigation. The author would like to thank Professors Yasuhiko Shirota and Koichi Niihara of Osaka University for reviewing this thesis and their valuable suggestions and comments. The author would like to express the deep appreciation to Dr. Nobuhito Imanaka for his helpuful advice. The author is very grateful to Dr. Ken-ichi Machida and Dr. Toshiyuki Masui for their valuable suggestions.

The author wishes to make grateful acknowledgment to Professor Fumikazu Kanamaru of Fukui Institute of Technology and Dr. Shinichi Kikkawa of Osaka University for their impressive discussions.

The studies have been carried out at Hyogo Prefectural Institute of Industrial Research. The author is very grateful to Dr. Genzo Hashizume and Dr. Satoru Nakagawa for giving the opportunity to start this investigation. The author appreciated to Dr. Muneyuki Motoyama for his guidance and encouragement throughout this research. Acknowledgments are made to Dr. Kayoko Amita, Dr. Hiroshi Matsui, Mr. Ken-ichi Ishima, Mr. Susumu Kawai, Dr. Tsuguo Ishihara and all the other members of Hyogo Prefectural Institute of Industrial Research for their helps.

Hideki YOSHIOKA